(12)

David Taylor Research Center
Bethesda, MD 20084–5000

DTRC–SME–89/79 October 1990
Ship Materials Engineering Department
Research and Development Report

Microstructural Features Controlling Ductile–to–Brittle Transition Behavior in High–Strength, Martensitic Steel Weld Metals

by
J. J. DeLoach, Jr.

DTRC–SME–89/79 Microstructural Features Controlling Ductile–to–Brittle Transition Behavior in High Strength, Martensitic Steel Weld Metals

MAJOR DTRC TECHNICAL COMPONENTS

CODE 011 DIRECTOR OF TECHNOLOGY, PLANS AND ASSESSMENT

12 SHIP SYSTEMS INTEGRATION DEPARTMENT

14 SHIP ELECTROMAGNETIC SIGNATURES DEPARTMENT

15 SHIP HYDROMECHANICS DEPARTMENT

16 AVIATION DEPARTMENT

17 SHIP STRUCTURES AND PROTECTION DEPARTMENT

18 COMPUTATION, MATHEMATICS & LOGISTICS DEPARTMENT

19 SHIP ACOUSTICS DEPARTMENT

27 PROPULSION AND AUXILIARY SYSTEMS DEPARTMENT

28 SHIP MATERIALS ENGINEERING DEPARTMENT

DTRC ISSUES THREE TYPES OF REPORTS:

1. **DTRC reports, a formal series,** contain information of permanent technical value. They carry a consecutive numerical identification regardless of their classification or the originating department.

2. **Departmental reports, a semiformal series,** contain information of a preliminary, temporary, or proprietary nature or of limited interest or significance. They carry a departmental alphanumerical identification.

3. **Technical memoranda, an informal series,** contain technical documentation of limited use and interest. They are primarily working papers intended for internal use. They carry an identifying number which indicates their type and the numerical code of the originating department. Any distribution outside DTRC must be approved by the head of the originating department on a case-by-case basis.

NDW-DTNSRDC 5602/51 (Rev 2-88)

UNCLASSIFIED

IRITY CLASSIFICATION OF THIS PAGE

REPORT DOCUMENTATION PAGE

REPORT SECURITY CLASSIFICATION classified	1b RESTRICTIVE MARKINGS
SECURITY CLASSIFICATION AUTHORITY	3 DISTRIBUTION / AVAILABILITY OF REPORT Approved for public release; distribution unlimited
DECLASSIFICATION / DOWNGRADING SCHEDULE	
ERFORMING ORGANIZATION REPORT NUMBER(S) TRC/SME-89/79	5 MONITORING ORGANIZATION REPORT NUMBER(S)
NAME OF PERFORMING ORGANIZATION avid Taylor Research Center	6b OFFICE SYMBOL (If applicable) DTRC 2815
7a NAME OF MONITORING ORGANIZATION	
ADDRESS (City, State, and ZIP Code) ethesda, MD 20084-5000	7b ADDRESS (City, State, and ZIP Code)
NAME OF FUNDING / SPONSORING ORGANIZATION avid Taylor Research Center	8b OFFICE SYMBOL (If applicable) Code 0115
9 PROCUREMENT INSTRUMENT IDENTIFICATION NUMBER	
ADDRESS (City, State, and ZIP Code) ethesda, MD 20084-5000	10 SOURCE OF FUNDING NUMBERS

PROGRAM ELEMENT NO	PROJECT NO	TASK NO	WORK UNIT ACCESSION NO
62234N			DN507603

TITLE (Include Security Classification)

U) Microstructural Features Controlling Ductile-to-Brittle Transition Behavior in High Strength, Martensitic Steel Weld Metals

PERSONAL AUTHOR(S)

.J. DeLoach, Jr.

TYPE OF REPORT	13b TIME COVERED FROM ____ TO ____	14 DATE OF REPORT (Year, Month, Day)	15 PAGE COUNT
		1989, October	122

SUPPLEMENTARY NOTATION

Submarine Materials Block
Work Unit No. 1-2815-909

COSATI CODES		
FIELD	GROUP	SUB-GROUP

18 SUBJECT TERMS (Continue on reverse if necessary and identify by block number)

High strength steel, Ductile-brittle transition
Martensitic, Mechanical properties
Weld metal

ABSTRACT (Continue on reverse if necessary and identify by block number)

An investigation of the transition behavior of high strength steel, martensitic weld metals was conducted. The objective of the investigation was to identify the specific microstructural features that control ductile-brittle transition in these weld metals. The approach systematically combined experimental measurements and observations with the use of analytical expressions. Charpy V-notch (CVN) properties, tensile properties, and cleavage fracture stress (σ_c) were generated over a range of temperatures. The critical tensile stress criterion (CTSC) was applied in the form of a modified Griffith-Orowan expression. To establish the applicability of the CTSC to the transition regime, transition temperatures were predicted from σ_c measurements, and compared to measured CVN transition temperatures.

(see reverse side)

DISTRIBUTION / AVAILABILITY OF ABSTRACT	21 ABSTRACT SECURITY CLASSIFICATION
☐ UNCLASSIFIED/UNLIMITED ☒ SAME AS RPT ☐ DTIC USERS	UNCLASSIFIED

NAME OF RESPONSIBLE INDIVIDUAL	22b TELEPHONE (Include Area Code)	22c OFFICE SYMBOL
Johnnie J. DeLoach, Jr.	301-267-5207	Code 2815

FORM 1473, 84 MAR 83 APR edition may be used until exhausted
All other editions are obsolete

SECURITY CLASSIFICATION OF THIS PAGE

☆ U.S. Government Printing Office: 1986—607-044

UNCLASSIFIED

Block 19. (Continued)

Results indicated that predicted transition temperatures showed good agreement with measured CVN transition temperatures. This agreement quantitatively demonstrated the dependence of transition temperature on σ_c, and verified the applicability of the CTSC in analyzing ductile-brittle transition behavior. CVN transition temperature and σ_c, were relatively insensitive to cooling rate. This suggested that the size of the controlling microstructural feature was also insensitive to cooling rate variations. Critical microcrack sizes, calculated from σ_c measurements, ranged from 0.5 to 1.5μm, typical of weld metal inclusion diameters. The insensitivity of transition temperature and σ_c to cooling rate and the calculated microcrack sizes suggested that nonmetallic inclusions were the controlling microstructural features. This was substantiated by fractographic observations of cleavage fracture stress specimens, which revealed that Ti-bearing inclusions, approximately 0.5 to 1.0μm in diameter, were associated with cleavage initiation.

These results are consistent with an inclusion-controlled mechanism and suggest that the transition behavior of high strength steel weld metals with predominantly martensitic microstructures depends critically on inclusion distribution.

ABSTRACT

An investigation of the transition behavior of high strength steel, martensitic weld metals was conducted. The objective of the investigation was to identify the specific microstructural features that control ductile-brittle transition in these weld metals. The approach systematically combined experimental measurements and observations with the use of analytical expressions. Charpy V-notch (CVN) properties, tensile properties, and cleavage fracture stress (σ_c) were generated over a range of temperatures. The critical tensile stress criterion (CTSC) was applied in the form of a modified Griffith-Orowan expression. To establish the applicability of the CTSC to the transition regime, transition temperatures were predicted from σ_c measurements, and compared to measured CVN transition temperatures.

Results indicated that predicted transition temperatures showed good agreement with measured CVN transition temperatures. This agreement quantitatively demonstrated the dependence of transition temperature on σ_c, and verified the applicability of the CTSC in analyzing ductile-brittle transition behavior. CVN transition temperature and σ_c were relatively insensitive to cooling rate. This suggested that the size of the controlling microstructural feature was also insensitive to cooling rate variations. Critical microcrack sizes, calculated from σ_c measurements, ranged from 0.5 to 1.5μm, typical of weld metal inclusion diameters. The insensitivity of transition temperature and σ_c to cooling rate and the calculated microcrack sizes

suggested that nonmetallic inclusions were the controlling microstructural features. This was substantiated by fractographic observations of cleavage fracture stress specimens, which revealed that Ti-bearing inclusions, approximately 0.5 to 1.0μm in diameter, were associated with cleavage initiation.

These results are consistent with an inclusion-controlled mechanism and suggest that the transition behavior of high strength steel weld metals with predominantly martensitic microstructures depends critically on inclusion distribution.

ACKNOWLEDGEMENTS

I extend my sincere gratitude to Dr. Robert E. Green for serving as my advisor and for his guidance and infinite patience. Additionally, I would like to thank Mr. Paul W. Holsberg and Dr. John P. Gudas for their technical support and personal encouragement. The technical advice and assistance of Dr. Ron W. Armstrong is gratefully acknowledged.

This work could not have been completed without the cooperation and assistance of many people. Sincere thanks go to Messrs. Brian A. Grachik, William A. Worden, Michael G. Vassilaros, Mark T. Kirk, Richard E. Link, Kyle C. Koppenhoefer, Albert V. Brandemarte, M. Frederick Dersch, Robert L. Mattox, and Ms. Florence T. Connell.

Very special thanks are extended to Messrs. Gene L. Franke, for his valuable technical advice and continual support, and Roy A. Lindauer, for his dedicated and diligent contributions. Your commitment was key to the completion of this work.

Finally, sincere love and gratitude is extended to my wife, Lauren, for her everlasting support and unending patience.

This research was funded by the Office of Naval Technology, Code 225 (Mr. James Kelly), through the David Taylor Research Center, Codes 0115 (Mr. Ivan L. Caplan) and 2800 (George A. Wacker).

This work is dedicated to Johnnie Sr., Thelma, Pamela, Jason, and Lauren.

TABLE OF CONTENTS

TABLE OF CONTENTS (Continued)

TABLES

FIGURES

FIGURES (Continued)

INTRODUCTION

Advances in steel metallurgy and plate processing have allowed metallurgists to produce high toughness, easily weldable plate with yield strengths over 900 MPa [Manganello et al., 1964]. Advances in analytical techniques and in modelling of fracture processes have led to improved fracture toughness in high strength steel plate. Excellent resistance to cleavage fracture allows their use in applications requiring thick sections, low temperatures, and high loading rates. Structural application of these materials increases load-bearing capacity and reduces material cost.

As technology pushes the strength of structural steels to higher levels, the welding metallurgist is presented with the difficult task of developing weld metals of equivalent and, in some applications, superior mechanical properties. By increasing weld metal hardenability and content of solid solution strengthening elements, it is relatively simple to achieve higher weld metal strength; however, maintaining good toughness at high strengths is exceedingly difficult [Masaluchi, 1966]. This problem renders many high strength steel welding consumables unfit for use in extreme service environments. Thus, the use of high strength steel plate is often limited by inferior fracture toughness properties of the welding consumables.

Knowledge of fracture processes in weld metal has not kept pace with that of steel plate and has resulted in an inadequate understanding of the mechanisms of fracture in high strength weld metals. Studies designed to improve the understanding of

metallurgical and micromechanical aspects of fracture in high strength steel weld metal are sorely needed. Until these studies are performed and a better understanding of fracture mechanisms in high strength steel weld metals is achieved, many of the advantages provided by the high strength, high toughness steel plate will not be realized.

The objective of this study was to identify the microstructural features that control ductile-brittle transition behavior of high strength, martensitic steel weld metals. The approach systematically combined experimental measurements and observations with the use of analytical methods. Mechanical property tests, as well as chemical, metallographic, and fractographic analyses were performed. The critical tensile stress criterion (CTSC) was applied analytically. To assess the applicability of the CTSC to the transition regime, transition temperatures were predicted from critical cleavage fracture stress measurements and compared to measured transition temperatures. Critical flaw sizes for elastic fracture, calculated from cleavage fracture stress measurements, were correlated with fractographic and metallographic observations to identify the microstructural features that control cleavage fracture resistance and ductile to brittle transition. This experimental design contrasts the traditional approach of developing qualitative and empirical correlations between fracture toughness and weld metal composition or microstructure, and represents a novel approach to the study of fracture properties of high strength steel weld metal.

The upcoming section reviews the critical tensile stress criterion and the ductile-brittle transition analysis used in this study. Included will be a discussion of the significance and physical meaning of cleavage fracture stress, as well as a derivation of the analytical expression used to relate cleavage fracture stress to transition temperature. Following this, a description of the metallurgy and properties of high strength steel weld metals will be presented. A review of previous studies that examined the metallurgical factors controll _ cleavage fracture resistance will follow. The review will focus primarily on we] metal studies; although work relating to cleavage fracture in high strength, martensitic steel plate will also be discussed. The approach will then be described, followed by a description of the plate, welding wires, and experimental procedures. Finally, results of all tests and analyses will be presented and the microstructural features controlling ductile-brittle transition behavior in high strength, martensitic steel weld metals will be discussed.

THEORY

CLEAVAGE FRACTURE STRESS AND THE CRITICAL TENSILE STRESS CRITERION

Cleavage fracture is a transgranular fracture mode that is most often seen in BCC metals and is generally associated with brittle, low-energy failure. A widely accepted model is that cleavage fracture initiates from microcracks at brittle particles, such as carbides, [Smith, 1966], pearlite [Kavishe and Baker, 1986], or nonmetallic inclusions [Tweed and Knott, 1983]. Figure 1 presents a schematic illustration of one possible cleavage process in steels. In the initial stage, local stress results in impingement of a dislocation array on a grain boundary particle. The particle cracks under the influence of the dislocation pile-up stresses, forming a microcrack. The critical and final stage in the fracture process occurs when a level of tensile stress is reached that causes the microcrack to propagate into the ferrite matrix. Thus, the requirements for cleavage fracture, as noted by Smith [1968], are plastic flow and a critical combination of particle size and local stress.

The preceding model, which describes a propagation-controlled mechanism, adheres to the critical tensile stress criterion (CTSC). That is, macroscopic cleavage fracture can occur only after a critical level of tensile stress is achieved. This critical tensile stress is termed the cleavage fracture stress. For slip-induced fracture, cleavage fracture stress is largely insensitive to temperature [Knott, 1966] and strain rate [Knott, 1976; Sandstrom and Bergstrom, 1984]. When fracture is

induced by twinning, cleavage fracture stress increases with temperature [Oates, 1969].

Orowan [1948] developed a theoretical model, based on Griffith's [1920] model for fracture of brittle solids, that related cleavage fracture stress, σ_c, to microcrack size and the plastic work expended in crack propagation. Orowan's model can be described using the following expressions [Orowan, 1948];

$$\sigma_c^2 = [\pi E(\gamma_s + W_p)]/2(1-\nu^2)r, \text{ penny-shaped crack} \quad (1)$$

$$\sigma_c^2 = [2E(\gamma_s + W_p)]/\pi(1-\nu^2)r, \text{ through-thickness crack} \quad (2)$$

where E is Young's modulus, ν is Poisson's ratio, γ_s is the surface energy of the matrix, W_p is the plastic work term, and r is the radius or half-thickness of the microcrack that can propagate at a stress equal to σ_c.

Smith [1966] later developed a model for the specific case of carbide-controlled fracture in mild steel. His model, which considered the combined effect of dislocation pile-up stress and applied stress on crack propagation, was expressed as

$$\frac{C_o}{d}(\sigma_c^2) + \tau_e^2 \left[1 + \frac{4}{\pi}\frac{\sqrt{C_o}}{\sqrt{d}}\frac{\tau_i}{\tau_e}\right]^2 \geq \frac{4E\nu_p}{\pi(1-\nu^2)d} \quad (3)$$

where C_o is the grain boundary carbide thickness, d is the average grain diameter, τ_e is the effective shear stress, τ_i is the lattice friction stress, and γ_p is the effective surface energy of ferrite. Curry and Knott [1978] restated the Smith model in terms of the grain size dependence of the effective shear stress. In published applications of the model [Knott, 1981; Bowen and Knott,

1984; Gudas, 1985], dislocation contribution generally has been neglected, reducing the expression to a modified form of the Griffith-Orowan equation

$$\sigma_c = [2\pi E\gamma_p/2(1-\nu^2)a]^{\frac{1}{2}}, \text{ penny-shaped crack} \quad (4)$$

$$\sigma_c = [4E\gamma_p/\pi(1-\nu^2)a]^{\frac{1}{2}}, \text{ through-thickness crack} \quad (5)$$

where a is the length of the microcrack and γ_p the plastic work term.

These Griffith-type models illustrate that σ_c, and thus cleavage fracture resistance, is inversely proportional to microcrack size. Metallographic studies by Allen et al. [1953], Low [1954], and McMahon and Cohen [1965] illustrated that microcracks can occur in specific microstructural features, such as ferrite grains and carbide films. As shown in the Smith model [1966], it then follows that σ_c is dependent on the size of the grains or particles contained within the microstructure. Rearranging Eqs. (4) and (5) gives

$$a = \pi E\gamma_p/(1-\nu^2)\sigma_c^2, \text{ penny-shaped crack} \quad (6)$$

$$a = 4E\gamma_p/\pi(1-\nu^2)\sigma_c^2, \text{ through-thickness crack} \quad (7)$$

which can be used to calculate microcrack sizes, if the cleavage fracture stress is known. Thus, the Griffith-type model can be used to determine the specific microstructural features that control the resistance to cleavage fracture initiation [Hahn, 1984]. A typical application involves measuring σ_c using notched bend or uniaxial tensile specimens. Critical microcrack size is then calculated from expressions such as Eqs. (6) or (7). Finally, the calculated sizes are then compared to the dimensions

of various microstructural features, arrested microcracks, or cleavage-initiating particles. This approach has been used successfully to explain the cleavage fracture behavior of many steels [Low, 1954; Brozzo et al., 1977; Curry and Knott, 1979; Bowen and Knott, 1984]. Due to its simplicity, widespread applicability, and the lack of an equivalent model for elastic-plastic fracture, the present study used the Curry and Knott expressions (Eqs. 4 through 7) to analyze the ductile-to-brittle transition behavior of high strength steel weld metals. However, because the CTSC and Griffith-type models define the condition for elastic fracture, its applicability to the problem of ductile-brittle transition, an elastic-plastic event, must first be established. One way of doing this is to verify a quantitative dependence of transition temperature on the cleavage fracture stress, σ_c. The following section describes the relationship between σ_c and transition temperature, and derives the expression used in the present study to analytically determine transition temperature from σ_c measurements.

RELATIONSHIP BETWEEN σ_c AND TRANSITION TEMPERATURE

The first widely accepted explanation for the relationship between cleavage fracture stress and the transition from ductile to brittle fracture was provided by Orowan [1945]. His theory, which was developed to explain the effect of a notch on the fracture behavior of mild steel, is illustrated in Fig. 2. The theory suggests that ductile-brittle transition is dependent upon the relationship between σ_c, assuming σ_c to be relatively

temperature independent, and yield stress. Referring to Fig. 2, specimens tested at temperatures above T_t fracture in a ductile manner because they yield at a stress level below the σ_c. Below T_t, fracture is brittle because the σ_c is reached before the specimen can yield. The stress intensification factor, Q, represents the local stress elevation due to specimen geometry. It is generally used to account for the presence of a V-notch.

Fig. 3 illustrates how σ_c and yield stress influence ductile-brittle transition. The figure shows that a decrease in σ_c, at a constant yield stress, or an increase in yield stress at a constant σ_c value, result in an increase in T_t.

From the basic Orowan theory, ductile-brittle transition temperatures can be expressed analytically as a function of yield stress and σ_c. One such analytical expression is derived below.

Armstrong [1964] expressed the relationship between σ_c and yield stress at ductile-brittle transition as:

$$\sigma_c = \alpha\sigma_y(T,\epsilon) \qquad (8),$$

where α is a stress intensification factor and a measure of the triaxial state of stress at the notch, T is temperature, and ϵ is strain rate. The yield stress, σ_y, can be expressed on a Hall-Petch basis [Hall 1951, Petch 1953] as;

$$\sigma_y = \sigma_o + k_y l^{-\frac{1}{2}} \qquad (9).$$

where σ_o is the friction stress and k_y is the Hall-Petch constant. The friction stress can then be written in terms of an athermal component, σ_G, and a thermal component, σ_{TH} [Armstrong et al., 1988];

$$\sigma_o = \sigma_G + \sigma_{TH} \quad (10),$$

where

$$\sigma_{TH} = B_o \exp-[\beta_o - \beta_1 \ln\epsilon]T \quad (11).$$

B_o, β_o, and β_1 are experimental constants evaluated in terms of dislocation model calculations [Armstrong, 1967]. Experimentally, B_o represents the value of σ_{TH} at T = 0°K. β_o and β_1 are determined from the strain rate dependence of slope values obtained from a plot of $\ln\sigma_{TH}$ versus temperature at various ϵ levels. Combining Eqs. (9) through (11) gives

$$\sigma_y = B_o \exp[\beta_o - \beta_1 \ln\epsilon]T + \sigma_G + k_y l^{-\frac{1}{2}} \quad (12).$$

This expression represents the temperature and strain rate dependent yield stress. By combining Eqs. 8 and 12 and setting $T = T_c$, the ductile-brittle transition temperature can be expressed as

$$T_c = [(\beta_o - \beta_1 \ln\epsilon)^{-1}][\ln(\alpha B_o) - \ln\{\sigma_c - \alpha(\sigma_G + k_y l^{-\frac{1}{2}})] \quad (13).$$

Armstrong et al., [1988] used this expression to analyze the transition behavior of controlled-rolled, microalloyed steels. Excellent agreement was obtained between T_c and measured CVN 50% FATT values over a range of grain sizes. Sandstrom and Bergstrom [1984] used a similar expression, neglecting the β_0 term, to calculate the CVN nil-ductility temperature of a C-Mn and a microalloyed steel. Equation 13 was used in the present study to verify a relationship between σ_c and ductile-brittle transition temperature for high strength steel weld metals.

BACKGROUND

CHARACTERISTICS OF HIGH STRENGTH STEEL WELD METAL

This study examines the cleavage fracture resistance and the ductile-brittle transition behavior of two high strength steel weld metals. Both weld metals are based on a low carbon, Ni-Cr-Mo-V alloy design, and are intended to exhibit yield stresses greater than 930 MPa. Because of the high strength requirement, the hardenability of the weld metal is sufficient to produce a predominantly martensitic structure over a large range of welding conditions. This section presents a review of the metallurgy and properties of this class of weld metal.

Alloy Design

The phases present in as-welded, weld metal microstructures are determined principally by composition and cooling rate. The influence of these factors is illustrated in Fig. 4, using schematic continuous cooling transformation diagrams. Increasing hardenability, by adding alloying elements such as carbon, manganese, and nickel, stabilizes the austenite phase, suppresses transformation to ferrite and bainite, and promotes martensite transformation. This is shown in Fig. 4a by a shift of the ferrite and bainite fields to longer times. Fig. 4b illustrates the influence of cooling rate on transformation. For a given composition, slow cooling rates favor formation of soft ferritic structures, whereas fast cooling rates favor the development of hardened, martensitic structures.

As mentioned earlier, a predominantly martensitic microstructure is needed to produce the high yield stresses exhibited by the weld metals examined in this study. The filler wires are alloyed to produce high hardenability, so that martensite will form over a wide range of cooling rates. The maximum strength and fracture toughness of the martensite is determined by the alloying elements present in the weld metal. The following paragraphs describe the role of the major alloying elements generally found in these weld metals.

Carbon is the primary strengthening agent; its level controls the maximum strength of the martensite [Winchell and Cohen, 1962]. Carbon content is generally between 0.05% and 0.09%. This is based on the work of Dorschu and Lesnewich [1964], who found that this range provided adequate strength without causing cracking and severe toughness degradation.

Manganese provides hardenability and is thought to increase impact toughness at levels up to 1.8% [Dorschu and Lesnewich, 1964]. Molybdenum and chromium are added to promote hardenability and to reduce softening during reheating in multipass welding. Nickel is added primarily to lower the ductile-brittle transition temperature. Vanadium is a potent strengthener, but is added in limited amounts because of its deleterious effect on weld metal toughness and hot cracking sensitivity. Titanium, aluminum, and silicon are used as deoxidants to control weld metal porosity.

Properties

Dorschu and Lesnewich [1964] performed the initial studies of the properties of high strength, Ni-Cr-Mo-V weld metals. Their work centered on developing filler metals that could achieve a room temperature yield stress of 965 MPa with good low temperature impact toughness. A filler metal composition was derived that produced a yield stress of 1055 MPa with a CVN energy of 69 J at -51°C. They reported that decreasing cooling rate, induced by increasing heat input and preheat, reduced yield stress and the 27 J transition temperature. Low-temperature bainite was identified as the microstructure required to retain high toughness in weld metals with yield stresses exceeding 965 MPa.

Enis and Telford [1968] later postulated that weld metal microstructures containing a high percentage of martensite were needed to achieve yield stresses greater than 965 MPa. They developed a filler metal for gas metal arc welding that exhibited a CVN energy of 70 to 80 J at -51°C with a yield stress of approximately 965 MPa. The composition of this filler metal was designed to produce a fully martensitic microstructure when deposited under typical shipyard conditions. Like Dorschu and Lesnewich [1964], they reported that yield stress dropped significantly with increases in heat input and preheat temperature; however, unlike the Dorshu and Lesnewich study, impact properties were insensitive to these variables. Carbon content was shown to have a dramatic effect on both yield stress and impact properties. Increasing carbon content from 0.095 to

0.110 raised the yield stress from 950 to 1030 MPa and decreased CVN energy at -18°C from 88 to 61 J.

Conner et al. [1967] examined the effect of preheat and cooling rate on the microstructures and mechanical properties of high strength steel weld metal. Results indicated that yield stress approached 1035 MPa at a cooling rate of approximately 33°C/s, and decreased to 895 MPa at a cooling rate of 18°C/s. Yield stress dropped dramatically at cooling rates below 18°C/s. The decrease in yield stress with decreasing cooling rate was accompanied by a change from a fine acicular microstructure to a coarse acicular structure containing free ferrite. The authors interpreted this as a transition from martensite to bainite, and suggested that the difference in strength was due to the change in microstructure. Charpy V-notch energy at -18°C was examined over the same cooling rate range as the yield stress. Results indicated that absorbed energy was not significantly influenced by cooling rate changes, although the maximum absorbed energy appeared to decrease with increasing cooling rate.

Saunders [1975] examined the influence of major alloying elements on the properties and microstructures of shielded metal arc welds with minimum yield stresses of 900 MPa. The effect of manganese, chromium, nickel, and molybdenum content on the strength and fracture toughness of as-deposited, single-pass welds was determined. Tensile and crack opening displacement (COD) tests were conducted over a temperature range of -196 to 22°C.

Results indicated that all of the microstructures contained varying mixtures of lath and autotempered martensite. The proportion of autotempered martensite decreased with increasing nickel content. This was attributed to the fact that increasing nickel reduces the martensite start temperature. All of the welds exhibited yield stresses of at least 900 MPa at room temperature, with yield stress to ultimate tensile stress ratios greater than 0.8. Yield stress was determined primarily by carbon content, and was insensitive to changes in nickel, chromium, manganese, and molybdenum contents. Nickel had a small beneficial effect on fracture toughness when initiation was by cleavage. Saunders observed no clear effect of chromium on fracture toughness and could not independently assess the influence of manganese and molybdenum. Fractographic observations indicated that quasicleavage fracture paths were altered, and occasionally arrested, by prior austenite grain boundaries. There were also indications that packet and lath boundaries caused small, but insignificant, perturbations in the fracture profile. In COD tests conducted above -100°C, an increasing amount of ductile-type fracture was observed on the specimen fracture surfaces. A zig-zag form of fracture propagation was observed in specimens that fractured in a totally ductile manner. Saunders suggested that propensity for this type of fracture exists in materials with high strength and low work hardening rates.

In a more recent study, Hasson et al. [1984] investigated the effect of welding procedures on the fracture toughness of as-

deposited 5-Ni steel weld metals. Elastic-plastic fracture toughness tests were performed on welds produced by both the gas metal arc (GMA) and gas tungsten arc (GTA) welding processes. Results indicated that the GTA weld metal displayed higher crack initiation energy and tearing resistance than 5-Ni steel base metal and GMA weld metal. Low heat input GTA welding conditions produced the highest fracture resistance. This was attributed to the refined microstructure that resulted from repeated reheating and tempering cycles experienced by the GTA weld metal. The GMA weld metal displayed lower fracture toughness properties than 5-Ni steel baseplate and the GTA weld metal. This was attributed primarily to the higher oxygen content of the GMA weld metal. Increasing heat input lowered the fracture toughness of the GTA weld metal, but raised the fracture toughness of the GMA weld metal. Though not discussed by the authors, the reason is likely linked to the effect of heat input on weld metal yield stress. For the GTA weld metal, a decrease in heat input from 2.6 to 1.4 MJ/m caused yield stress to increase minimally from 1000 to 1014 MPa. Meanwhile, the fracture toughness increased because of the finer, heavily tempered microstructure associated with the lower heat input weld. Conversely, the yield stress of the GMA weld metal increased from 869 to 993 MPa when the heat input decreased from 3.2 to 1.8 MJ/m. The large increase in the strength of the weld metal apparently offset the effects of any microstructural refinement, causing the fracture toughness to decrease.

The latest work on the properties of high strength steel, predominantly martensitic weld metals was performed by Oldland [1988], who evaluated the effects of heat input and molybdenum content on the properties and microstructure of submerged arc welds. Heat input was varied from 1.2 to 3.8 MJ/m and molybdenum content from 0.5 to 0.9%. Tensile, hardness, and CVN tests were conducted and microstructural and fractographic examinations were performed.

Results indicated that microstructure changed from autotempered lath martensite at a heat input of 1.2 MJ/m to a mixture of martensite, bainite, and retained austenite at heat inputs of 2.5 and 3.8 MJ/m. Increased heat input resulted in decreased strength and hardness and increased impact toughness and ductility. Molybdenum was shown to increase the proportion of martensite observed at the higher heat inputs. Additionally, as molybdenum content increased, hardness and tensile ductility increased; whereas impact toughness decreased. The decrease in toughness with increasing molybdenum was attributed to an increase in lath packet size.

MICROSTRUCTURAL FEATURES CONTROLLING CLEAVAGE FRACTURE

The following section reviews some of the recent work in identifying the micromechanisms of cleavage fracture in weld metals and in martensitic microstructures. Each study that will be reviewed focused on identifying specific microstructural features controlling cleavage fracture. Many of the

investigations employed a combined experimental/analytical approach similar to that used in the present study.

Modelling of the fracture processes of weld metals is relatively new, and work has been limited, especially in comparison to the abundance of work that has been done on plate. Initial examinations of weld metals have concentrated primarily on ferritic microstructures, with little work being performed on martensitic weld metals. The weld metal studies discussed in this section were conducted on C-Mn steel types. These weld metals have ferritic microstructures and have much lower strength levels than the weld metals examined in the present investigation. Due to the lack of previous work on martensitic weld metals, a review of some previous studies performed on high strength, martensitic steel plate will also be presented.

Weld Metal Studies

Tweed and Knott [1983] examined the effects of reheating on the fracture toughness of C-Mn weld metal. Shielded metal arc welds were reheated to 900 and 1250°C to generate the fine and coarse reheated regions typically observed in multipass welds. Crack opening displacement (COD) tests were conducted at -40, 0, and 22°C.

The as-welded microstructure was comprised predominantly of acicular ferrite, with some grain boundary ferrite also present. The 1250°C reheating treatments reduced the amount of acicular ferrite and increased the amount of grain boundary ferrite. After reheating the as-welded material to 900°C, the microstructure

contained only grain boundary ferrite. In general, reheating reduced prior austenite and ferrite grain size. Microhardness tests indicated that the acicular ferrite had higher hardness than grain boundary ferrite. COD toughness was higher for the reheated weld metal, especially at the 0°C test temperature. Fractographic observation indicated that cleavage fracture initiation generally occurred at a nonmetallic inclusion lying on a large, brittle facet that was typically associated with grain boundary ferrite. Crack paths typically followed grain boundary ferrite.

From these observations Tweed and Knott proposed the following tentative model for brittle fracture in as-welded microstructures. On deformation, plasticity is initially localized in grain boundary ferrite because it is the softer of the phases present. Dislocations pile-up or tangle around inclusions, leading to some cracking. At a critical combined level of dislocation stress and applied stress, one or more cracks grow to give brittle failure. Based on this model, the authors stated that weld metal toughness depended critically on the size of inclusions and their proximity to the fatigue precrack tip. Further they concluded that brittle fracture is favored by large grain size, due to increased pile-up stresses; high yield stress and work hardening exponents, due to enhanced crack tip stresses; and large inclusions, due to lower crack propagation stresses. This model was later applied successfully by McRobie and Knott [1985] to explain the effect of strain and strain aging on C-Mn weld metal toughness.

Tweed and Knott [1987] used the inclusion-control model in an examination of the effect of preheat on the fracture toughness of C-Mn weld metals. Four shielded metal arc weldments were produced using preheat temperatures of 200, 20, and -50°C (two plates at -50°C). Crack tip opening displacement (CTOD) tests were performed, using side-notched specimens in pure four-point bending, at -10°C. Tensile tests were performed at temperatures ranging from -140°C to ambient.

Results indicated that the width of columnar prior austenite grains, acicular ferrite grain size, grain boundary ferrite grain size, and the proportion of grain boundary ferrite increased with increasing preheat temperature. Weld metal hardness and microhardness decreased with increasing preheat. Both yield stress and ultimate tensile stress decreased with increasing preheat temperature. CTOD for stable crack growth, δ_i, was virtually independent of preheat temperature. The -50 and 200°C preheats led to some specimens failing by cleavage; whereas the 20°C preheat resulted in no cleavage failures.

Fractographic examination revealed that all specimens showed some microvoid coalescence. Cleavage initiation sites were identified at two pop-ins, one from each of the -50°C preheat welds, and at an isolated area of cleavage on the fatigue precrack of a specimen from the 200°C preheat weld. Cleavage initiation in one of the pop-ins and in the cleavage area on the fatigue precrack were associated with large (~2μm) cracked inclusions. No specific initiating particle could be identified for the second

pop-in, but a cluster of small inclusions were noted in the vicinity of the initiation site. A bimodal facet size distribution was observed on cleavage fracture surfaces. Large facets were generally associated with grain boundary ferrite, although isolated instances of cleavage across ferrite sideplate colonies were also noted. Small facets were generally associated with acicular ferrite.

To explain the brittle fracture performance of the welds, critical crack propagation stresses were predicted by modelling the cracked inclusions as circular Griffith cracks using the following expression

$$\sigma_c = (\pi/2)[2E\gamma_p/\pi(1-\nu^2)a]^{\frac{1}{2}} \qquad (14).$$

The material properties and inclusion size distributions were assumed to be similar for all welds tested, resulting in equivalent predicted values for σ_c. Thus, the fracture toughness properties were expected to scale with the maximum expected crack tip stresses, which are a function of yield stress and work hardening properties. The data showed that this was not consistent the minimum CTOD values for brittle failure at -10°C, which were used to characterize brittle fracture properties. Specifically, the -50°C preheat and 200°C preheat welds had similar brittle fracture properties, but very different yield stresses, and thus very different predicted maximum crack tip stresses. Tweed and Knott suggested that one possible problem was that the critical crack propagation stress model did not include the influence of dislocation pile-up stresses. They proposed that

the pile-up stress increased with increasing preheat temperature because of an increase in grain size, and that, for a similar-size initiator, the critical propagation stress should decrease. Thus, the higher available crack tip stress for the low preheat material may have been balanced by a lower critical propagation stress in the high preheat material, resulting in similar fracture properties.

Chen and Yan [1988] examined the effect of manganese and acicular ferrite contents on the microfracture behavior of multipass, C-Mn steel weld metal. Charpy V-notch tests were conducted at -60°C on shielded metal arc welds with manganese levels ranging from 0.68 to 1.98%. Results indicated that the proportion of acicular ferrite increased with increasing manganese content. Charpy V-notch energy increased with manganese up to 1.54%, but decreased when manganese was raised to 1.98%. Fractographic observations indicated that a region of fibrous cracking occurred immediately adjacent to the notch tip. The maximum width of the fibrous cracks were measured and found to increase with increasing toughness. Cleavage cracks initiated a few hundred micrometers ahead of the fibrous region. Cleavage initiation occurred at various types of second phase regions, including M-A constituent, pearlite colonies, and nonmetallic inclusions. In all cases, the initiation sites were surrounded by several cleavage facets totalling approximately 40-50μm in diameter. Chen and Yan stated that this terrace of cleavage facets was formed by propagation of the original cleavage crack

into neighboring ferrite grains. Metallographic examinations revealed that the region of cleavage initiation was characterized by coarse ferrite grains.

Based on these results, the authors proposed the following mechanism for cleavage fracture at -60°C. As the strain at the notch tip exceeded a critical value, a fibrous crack initiated and propagated. The stress ahead of the notch increased until, with the addition of dislocation-induced stresses, a cleavage crack initiated at a second-phase particle. The crack then extended into neighboring ferrite grains. If the normal stress exceeded the local fracture stress, the crack continued to propagate, causing complete specimen fracture. The local fracture stress was considered to be modified by the size of the ferrite crack; larger ferrite cracks allowed the critical fracture stress to be reached at a lower applied load. This permitted the cleavage crack to initiate and propagate earlier, resulting in a shorter fibrous crack region and reduced impact toughness. The beneficial effect of acicular ferrite was attributed to the decrease in the ferrite grain size.

Plate Studies

Naylor [1979] examined the influence of lath morphology on ductile-brittle transition in five martensitic-bainitic steels. Various austenitizing temperatures and cooling rates were used to vary lath width, packet diameter, and the proportions of martensite and bainite. Room temperature tensile properties and

CVN ductile-brittle transition temperatures (DBTT) were determined for each material condition.

Results indicated that DBTT decreased as packet diameter and lath width decreased and that major cleavage crack deviations occurred at packet boundaries. From this Naylor proposed that lath width and packet diameter controlled cleavage fracture of martensitic-bainitic steels. His model for quasicleavage fracture permitted small crack front deviations across laths, with establishment of another crack plane at packet boundaries. A Griffith-type fracture stress criterion was developed that included a logarithmic function of the inverse square root of the product of packet diameter and lath width.

In a study of the micromechanisms of cleavage fracture in HY-80 steel, Hagiwara and Knott [1981] also concluded that packet diameter controlled the cleavage fracture resistance of martensitic-bainitic steels. Specimens were austenitized and quenched to produce 100% martensite, or austenitized and isothermally transformed to produce varying proportions of upper bainite. Fracture toughness and cleavage fracture stress tests were performed on each material condition.

Fracture toughness decreased with small percentages of bainite, and remained constant at bainite levels greater than 50%. The critical cleavage fracture stress also decreased with increasing bainite content, until reaching a constant value at bainite levels greater than 40%. Fractography revealed that the average diameter of cleavage facets in martensite and bainite were

10μm and 39μm, respectively. The critical fracture event was taken as propagation of a microcrack into an adjacent packet. The authors concluded that the influence of the proportion of bainite on fracture toughness was statistical in nature. Specifically, an increase in the amount of bainite increased the probability of having coarse bainitic packets in regions of high stress. Cleavage initiation at these coarse packets increased the microcrack size, which decreased the critical fracture stress, and resulted in reduced fracture toughness.

Bowen and Knott [1984] examined the effect of austenitizing temperature on the cleavage fracture stress and fracture toughness of A533B pressure vessel steel in the martensitic condition. Samples were austenitized at 900 and 1250°C for 1 hr and oil quenched. Fracture toughness tests, performed in four-point bending, were conducted over a temperature range of -196 to -60°C. Cleavage fracture stress tests were performed over a range of -196 to -100°C. Prior austenite grain sizes, lath packet sizes, autotempered carbide widths, and lath widths were measured for each material condition.

Metallographic examination showed that prior austenite grain size and packet size increased with austenitizing temperature. Packet size was found to be strongly dependent on prior austenite grain size. Autotempered carbide size and lath width did not vary significantly with prior austenite grain size. Cleavage fracture stress was independent of prior austenite grain size and packet size. Cleavage fracture stress was also independent of

temperature over the range of -100 to -160°C, supporting a tensile stress-controlled mechanism. K_{IC} values increased and transition temperature decreased with increasing prior austenite grain size and packet size.

Bowen and Knott attempted to explain these results using several potential micromechanisms of fracture. Possible critical stages in the fracture process were identified as propagation of a microcrack the size of; a martensite packet, an autotempered carbide, or a martensite lath. Martensite packets were discounted as the controlling microstructural feature because packet size varied significantly with prior austenite grain size; whereas cleavage fracture stress remained constant. Autotempered carbides were considered unlikely, because of their small size, unless extreme local stress elevations occurred from dislocation arrays. Because of the unlikeliness of a lath/lath interface arresting a running crack, martensite lath width also was eliminated as a controlling factor. The authors concluded that the observed K_{IC} and cleavage fracture stress values were consistent with an inclusion-controlled fracture mechanism.

Bowen and Knott [1986] later used the same material to examine the effect of specimen size on the cleavage fracture stress. For coarse-grained material, cleavage fracture stress decreased with increased specimen size and notch angle. This was attributed to an increase in sampling volume. The effect of specimen size and sampling volume on cleavage fracture stress was significantly reduced in the fine-grained material. These results

were consistent with the location of microcrack nuclei at prior austenite grain boundaries. For the coarse-grained condition, the micromechanism of failure was postulated as nucleation and propagation of microcracks from autotempered carbides located on widely spaced, embrittled prior austenite grain boundaries. For fine-grained, martensitic microstructures, the authors stated that the micromechanism of failure may involve the nucleation and propagation of microcracks from the coarsest autotempered carbides located at prior austenite grain boundaries or within grains.

APPROACH

The objective of this study was to determine the microstructural features that control the ductile-brittle transition behavior of high strength steel weld metals with predominantly martensitic microstructures. The traditional approach to studies such as this has been to develop empirical and qualitative correlations between toughness and composition or microstructure. Typically, CVN properties and compositions are determined, and microstructure is evaluated, at two or more conditions. Variations in CVN properties are then related to the observed differences in composition and microstructure. In many instances, this approach does not describe a mechanism of fracture and is unable to identify the specific microstructural features controlling fracture resistance.

The approach used in the present study attempted to surmount these shortcomings by systematically combining experimental measurements and observations with the use of analytical expressions. The various phases of the analysis are explained below.

Initially, a metallurgical characterization was performed to determine the weld metal compositions and microstructural characteristics. Following this, the tensile properties, CVN transition temperatures, and cleavage fracture stress were measured. In the next phase of the analysis, the dependence of transition temperature on cleavage fracture stress was verified using Eq. 13. Ductile-brittle transition temperatures were

calculated from cleavage fracture stress measurements and compared to measured CVN transition temperatures. This stage of the analysis established the applicability of the CTSC to the study of ductile-to-brittle transition, an elastic-plastic fracture event. Following this, the size of the cleavage-nucleating microcrack was calculated from cleavage fracture stress measurements using Eqs. 4 through 7, the modified Griffith-Orowan equations. As mentioned in the introductory discussion of the CTSC, calculated sizes have been shown to approximate the size of the microstructural feature that controls cleavage fracture. Finally, from the calculated sizes, and results of microstructural and fractographic evaluations, the specific microstructural features controlling ductile-brittle transition temperature were identified.

MATERIALS

The base metal used for all welds was 2.5-cm thick, low carbon, 5% Ni-Cr-Mo-V steel plate. The chemical composition is given in Table 1.

Two 1.6-mm diameter, bare filler wires were used for this investigation, designated wires A and B. These wires were chosen because both previously produced martensitic weld metals with yield stresses greater than 900 MPa over a wide range of welding conditions [Oldland, 1988]. Chemical compositions of sample lengths of the wires are presented in Table 1. Both wire compositions are based on a low carbon, Ni-Cr-Mo-V alloy design and depend upon carbon, manganese, chromium, molybdenum, and

vanadium for strength and hardenability. Nickel is added primarily to enhance low temperature toughness. Though the wires have the same basic compositional design, there are slight differences in the alloying strategies. Wire A contains more carbon, manganese, chromium, and vanadium, and less molybdenum and nickel than wire B. It appears that, when alloying for strength and hardenability, the designers of wire B reduced the content of elements that dramatically reduce toughness, such as carbon, chromium, and vanadium, in favor of molybdenum and nickel.

EXPERIMENTAL PROCEDURES

WELDMENT PREPARATION

Six 2.5 x 15 x 215-cm sections of 5% Ni-Cr-Mo-V steel were oxyacetylene flame cut from larger 2.5-cm thick plate. The plate edges were prepared and tack-welded together to produce the butt-joint configuration shown in Fig. 5. The 45° included angle and 1.25-cm root opening were selected to provide undiluted weld metal at mid-width of the joint.

Using the gas metal arc welding process, three multipass welds were produced in the flat position, using welding conditions shown in Table 2. Two sets of heat inputs and preheat/interpass temperatures were used. The welding variables were selected to ensure that the two resulting cooling rates were significantly different, yet fast enough to produce a high percentage of martensite. Wire A was used to produce both a high and low cooling rate weldment; whereas wire B was used to produce a high

cooling rate weldment only. The intent of this test matrix was to isolate the effects of cooling rate and composition.

Cooling rates at 537°C (1000°F) were measured by plunging unsheathed, Chromel-Alumel thermocouples into the molten weld metal at midlength of each weld pass. Temperature-time traces were recorded on an X-Y plotter. The cooling rate was taken as the tangent to the cooling curve at 537°C. The averages of the measured cooling rates are presented in Table 2. The weld identification scheme indicates the welding wire and cooling rate combination used to produce each weld. For example, the weld produced using wire A at a weld metal cooling rate of 28°C/s is referred to as weld A28.

WELD METAL EVALUATION

The filler metals and welding conditions described above were selected to (1) produce microstructures with a high percentage of martensite, and (2) isolate the effects of cooling rate and composition. The first stage of the weld metal evaluation characterized the compositions and microstructures to ensure that these were conditions were achieved. Weld metal chemical analyses were performed on material removed from the undiluted weld metal located at the approximate mid-width each weld. Optical microscopy was performed to determine prior austenite grain size and to characterize the microstructures of the last-bead and reheated regions of the welds. Samples, removed from locations shown in Fig. 6, were sectioned, mounted, and mechanically polished to 1 μm. To reveal prior austenite grain

boundaries, the samples were etched using a modified Winsteards solution. This solution is prepared as follows. Mix 4 g of picric acid in 20 ml ethanol; then add 400 ml H_2O; finally, add 10 g of sodium dodecylbenzene sulfonate. Grain size measurements were made using the circular intercept method at 280X magnification. To reveal microstructural phases, the samples were etched for 30 s in 4% picral, followed by 10 s in 2% nital, and then 20 s in 8% metabisulfate. A Zeiss Axiomat light metallograph was used for all metallographic examinations. Additionally, microhardness tests were performed on the last-bead and reheated regions of each weld. Measurements were made with a diamond pyramid hardness tester using a 1 kg load. Prior to testing, the samples were polished to 1μm and etched in 2% nital solution.

Tensile tests were performed over a temperature range of -196 to 22°C, using 6.4-mm diameter, all-weld-metal tensile bars. All tensile tests were performed in accordance with ANSI/AWS B4.0, using a crosshead speed of approximately 0.6 mm/min. All reduced temperature tests were performed in a closed chamber that was cooled by a jet of liquid nitrogen sprayed into the volume surrounding the specimen. A copper-constantan thermocouple, peened into a dummy specimen, was used to monitor test temperature. Ultimate tensile stress, 0.2% yield stress, and reduction of area were determined for each specimen.

Cleavage fracture stress tests were performed using notched bars of dimensions shown in Fig. 7. Notches were placed such that crack propagation occurred along the weld centerline, in undiluted

weld metal. Figure 8 illustrates the location from which the specimens were removed as well as the specimen orientation. Tests were performed using an ATS servo hydraulic test machine. The specimens were loaded in four-point bending at an approximate rate of 1 mm/min. Load and deflection were monitored until fracture using a load cell and deflectometer. Measurements were plotted using an X-Y recorder. Testing was conducted over a temperature range of -101 to -196°C. The tests were performed in a closed chamber cooled by a jet of liquid nitrogen sprayed into the volume surrounding the specimen. Copper-constantan thermocouples were attached to each specimen, and the leads were directed out of the chamber through an access port. Temperature was manually controlled to within 1.5°C using a needle valve. The following paragraph describes how cleavage fracture stress was determined from the experimental data.

The nominal bending stress, σ_{nom} was calculated from the fracture load using the following equation:

$$\sigma_{nom} = 1.5P_{max}l/Bb^2 \qquad (15),$$

where P_{max} is the fracture load, l is the loading span, B is the specimen thickness, and b is the remaining ligament under the notch. Equation 15 is derived by combining expressions for σ_{nom} and bending moment, M;

$$\sigma_{nom} = 6M/Bb^2 \qquad (16),$$

$$M = (P_{max}/4)l \qquad (17).$$

Values of σ_{nom} were then normalized with respect to yield stress, σ_y, determined at the same temperature. Each value of σ_{nom}/σ_y has a corresponding value of stress intensification, R, which can be expressed as

$$R = \sigma_{11}(max)/\sigma_y \qquad (18).$$

The variation of R with σ_{nom}/σ_y for the notched bar shown in Fig. 7, was determined by Griffiths and Owen [1971] using a two-dimensional stress analysis, and is presented in Fig. 9. By locating σ_{nom}/σ_y on the abscissa, the corresponding value of R was read from the ordinate. The cleavage fracture stress, σ_c, was taken to be equal to $\sigma_{11}(max)$, the product of the stress intensification and yield stress;

$$\sigma_c = \sigma_{11}(max) = R\sigma_y \qquad (19).$$

Charpy V-notch tests were performed on standard specimens at temperatures ranging from 65 to -118°C. The specimens and test procedures were in accordance with ANSI/AWS B4.0. Specimen orientation and location, relative to weld zone width and thickness, were the same as those used for the notched-bend specimens (see Fig. 8). All tests were conducted using a RIEHLE Model PI-2 test machine.

Fractography was performed using a JEOL Model JSM 35 scanning electron microscope. CVN specimens were examined to characterize ductile and brittle fracture modes. Notched-bend specimens were examined to identify fracture initiation sites.

RESULTS AND DISCUSSION

METALLURGICAL EXAMINATION

The intent of this study was to examine the ductile-brittle transition behavior of steel weld metals with martensitic structures. Welding conditions and filler metals were selected to produce predominantly martensitic microstructures and to isolate the effects of composition and cooling rate. To ensure that the desired weld metal compositions and microstructures were produced, and to gain a general characterization of the materials, a metallurgical examination of each weld metal was performed.

Composition

Weld metal compositions are presented in Table 3, along with calculated carbon equivalents. Carbon equivalents (C_{eq}) were calculated using the International Institute of Welding (IIW) formula;

$$C_{eq}(IIW) = C + Mn/6 + (Cr+Mo+V)/5 + (Cu+Ni)/15 \qquad (20)$$

where all amounts are in weight percent.

The major alloying elements found in the weld metals were carbon, nickel, manganese, chromium, and molybdenum. Welds A28 and A44 had very similar compositions, which was expected because both welds were deposited using filler wire A. The only differences between the two welds were slightly higher amounts of carbon and nickel in weld A28. Comparing these welds with weld B44 indicates that welds A28 and A44 had more carbon, chromium, and slightly more manganese; whereas weld B44 contained more nickel and molybdenum. These variations are consistent with the

previously-discussed differences in filler wire compositions and alloying strategies. Comparing the content of trace elements, we see that welds A28 and A44 had more vanadium than weld B44; whereas weld B44 had slightly more titanium. Aluminum and silicon contents were approximately the same for the three welds. The contents of impurity elements are also shown in Table 3. Welds A28 and A44 had similar levels of sulfur, phosphorus, and oxygen. Weld B44 had slightly less sulfur and phosphorus than welds A28 and A44.

The C_{eq} values for welds A28, A44, and B44 were 0.85, 0.83, and 0.78, respectively. These values are indicative of very high hardenability, which is necessary to achieve martensite over a wide range of welding conditions. The higher values displayed by welds A28 and A44 were due primarily to increased carbon, manganese, chromium, and vanadium contents.

Inclusion contents were estimated from the weld metal compositions using a method developed by Bailey [1978]. The method is outlined in Appendix A. The results, shown in Table 4, indicate that the calculated total inclusion contents were similar for the three welds. Weld B44 had a lower calculated sulfide content than weld A28 and weld A44, due to its lower sulfur content. Because of its higher titanium content, weld B44 had a higher calculated titanium oxide content than welds A28 and A44. The calculated aluminum oxide contents were similar for the three welds. Weld B44 had a lower calculated manganese silicate content than welds A28 and A44, despite having a similar oxygen content.

This was due to Bailey's assumption that oxygen combines with titanium and aluminum first, and that any remaining oxygen then forms manganese silicates. Weld B44 had a higher combined level of titanium and aluminum, leaving less oxygen for manganese silicate formation.

Microstructure

Table 5 presents the prior austenite grain sizes for the last bead and reheated regions of welds A28, A44, and B44. As previously illustrated in Fig. 6, the measurements were taken from the area corresponding to the notch root region of the bend and CVN specimens. The prior austenite grain sizes of the three welds were equivalent in both the last bead and reheated regions. As expected, reheating had little effect on prior austenite grain size.

Figures 10 through 12 present typical microstructures for the last-bead regions of welds A28, A44, and B44. The microstructures of the three welds were similar, all comprised primarily of a fine, acicular structure typical of autotempered lath martensite. Because of the difficulty in identifying low-temperature transformation products by optical microscopy, thermal data and microhardness data were used to substantiate this observation.

Previous dilatometric studies of Ni-Cr-Mo-V weld metal indicated that cooling rates greater than 8°C/s result in fully martensitic microstructures [Krantz, 1971; Holsberg, 1988]. This is much slower than the 28 and 44°C/s cooling rates used in the

present study, and suggests that the last-bead regions should be fully martensitic. As further evidence, diamond pyramid hardness (DPH) readings were taken within the last-bead region of each weld. These data, presented in Table 6, compare favorably to the microhardness values reported by Oldland [1988] for high strength steel weld metals with martensitic microstructures.

Martensite start (M_s) temperatures, estimated from the compositions using the following expression by Andrews [1965]

$M_s(°C) = 539-423(C)-30.4(Mn)-17.7(Ni)-12.1(Cr)-7.5(Mo)$ (21),

were found to be approximately 425°C. The high M_s temperatures, which show good agreement with dilatometric measurements of 405°C $\pm$ 15°C [Holsberg, 1988] and 415°C [Krantz, 1971] reported in the literature for Ni-Cr-Mo-V, high strength steel weld metals, suggest that autotempering of the martensite probably occurred upon cooling.

Thus, optical microscopy, cooling rate data, dilatometric information generated in previous studies, microhardness measurements, and calculated M_s temperatures suggest that the last-bead regions were comprised primarily of autotempered martensite. Though the microstructures appeared identical at the magnifications used, the microhardness data indicates that there may be slight differences. The slightly lower DPH value for weld A28, in comparison to weld A44, suggests that an increased amount of autotempering probably occurred in weld A28, due to its slower cooling rate. Comparing weld A28 to weld B44, we see that the increased autotempering of weld A28 offset its higher carbon

content, and resulted in equivalent microhardness values for these two welds. Weld B44 had a lower microhardness than weld A44, despite being produced using the same welding conditions. This can likely be attributed to the lower carbon content in weld B44. In addition, the lower C_{eq} of weld B44 suggests that it may contain a higher percentage of softer, non-martensitic phases than weld A44.

Typical microstructures observed in reheated regions of the welds are presented in Figs. 13 through 15. These micrographs are representative of the area directly below the center of the last bead. This area was of interest because it, along with a portion of the last bead, comprised the microstructure at the root of the notch of the CVN and bend specimens. Again, the structures were very similar and appeared to be predominantly martensitic. DPH measurements, presented in Table 6, show that the reheated regions were slightly softer than the last-bead regions. Although the reheated regions showed lower hardness, the levels were indicative of a predominantly martensitic microstructure. The reduction in hardness was caused by tempering of the martensite during deposition of subsequent passes and by probable transformation of a small percentage of bainite in re-austenitized regions. These observations, coupled with observations of the last-bead regions, suggest that the reheated weld metal was composed primarily of tempered and autotempered martensite, possibly with small amounts of bainite also present. Previous microstructural studies performed on high strength steel weld metals with compositions

similar to those studied herein [Holsberg, 1988; Oldland, 1988; Ramsey et al., 1989] support these findings. The effect of cooling rate and compositional differences was not visible in the reheated regions at the magnifications used. It is likely that scanning or transmission electron microscopy will be necessary to determine any microstructural variations.

Summary

A metallurgical characterization of the three welds was performed to ensure that the filler wires and welding conditions used in this study were sufficient to; (1) isolate the influence of cooling rate and composition, and (2) produce microstructures with a high percentage of martensite. The results of the chemical analyses indicate that the first condition was met. Welds A28 and A44, produced at different cooling rates, had the same nominal composition. Welds A44 and B44, produced at the same nominal cooling rate, had significantly different compositions. The results of optical metallography, thermal data, and microhardness measurements indicated that the three welds possessed primarily martensitic microstructures. The last-bead region was composed largely of autotempered martensite, due to the relatively fast cooling rates and high M_s temperatures. The reheated regions were a mixture of tempered and autotempered martensite, possibly with small amounts of bainite also present.

MECHANICAL PROPERTIES

Tensile Properties

Table 7 presents the results of tensile tests performed over a range of temperatures. Figure 16 presents the yield stress data as a function of temperature for the three welds. At room temperature, welds A28, A44, and B44 had yield stresses of 993 MPa 1055 MPa, and 1000 MPa, respectively. As temperature decreased, the yield stress of weld A44 continued to be 5 to 10% higher than that of welds A28 and B44. All of the welds showed an increase in yield stress as test temperature decreased. This behavior is common to BCC metals and is due to the increase in the Peierls-Nabarro stress and concomitant decrease in dislocation mobility as temperature decreases [Conrad, 1970]. The data in Fig. 16 show similar slopes, indicating that the temperature dependence of yield stress was approximately equal for the three welds. Specifically, welds A44 and B44 showed an elevation of approximately 26% from 22 to -196°C. Weld A28, not tested at -196°C, displayed a 10% elevation from 22 to -157°C, compared to approximately 15% for welds A44 and B44.

Comparing welds A28 and A44 indicates that the slower cooling rate of weld A28 resulted in a lower yield stress. The reduction in strength for weld A28 occurred because its lower cooling rate increased the amount of autotempering and the degree of tempering from subsequent weld beads. Previous studies have demonstrated the same effect of cooling rate on the yield stress of high strength steel weld metal. Dorschu and Lesnewich [1964]

found that increasing the cooling rate from 33°C/s to 79°C/s, resulted in an increase in room temperature yield stress from 879 to 1010 MPa. Additionally, they found that reducing the cooling rate by increasing preheat from 27 to 93°C caused the yield stress to drop from 1055 to 897 MPa. Conner et al. [1967] studied the effects of cooling rate on the mechanical properties of several heats of Ni-Cr-Mo-V weld metal. They found that yield stress approached 1034 MPa at cooling rates of approximately 33°C/s, decreased to approximately 930 MPa at 17°C/s, and dropped dramatically at cooling rates below 17°C/s.

Weld A44 also had a higher yield stress than weld B44, though both were produced at the same nominal cooling rate. In this case, the variation in yield stress was caused by compositional differences. Because the weld metals are predominantly martensitic, their strength depends largely on carbon content [Winchell and Cohen, 1962; Saunders, 1975]. Thus, the higher yield stress displayed by weld A44 is attributed to its higher carbon content. In addition, weld A44 had more vanadium than weld B44. Small additions of vanadium produce dramatic increases in strength and hardness [Dorschu and Stout, 1961; Dorschu and Lesnewich, 1964; Nakayama et al., 1968]. The higher content of other solid solution strengthening elements, such as chromium and manganese, may also have contributed to the strength difference.

Fig. 17 presents ultimate tensile stress (UTS) as a function of temperature. The data indicate very little difference in UTS

between the three welds. At room temperature, weld A44 had a UTS of 1140 MPa, compared with 1095 MPa for weld A28 and 1075 MPa for weld B44. Weld A44 was approximately 5% higher than weld A28 at room temperature; however, this difference decreased with decreasing temperature until, at -157°C, no difference existed. Weld A44 was also approximately 5% higher than weld B44 at room temperature, and maintained this difference over the entire test temperature range.

As was the case with yield stress, UTS increased with decreasing test temperature. Welds A44 and B44 showed 27 and 28% elevation from 22 to -196°C, respectively. This is similar to the yield stress temperature dependence. Weld A28 showed an elevation of 22% from 22 to -157°C, compared to a 10% increase in yield stress over the same temperature range.

Fig. 18 presents the yield stress to UTS ratios as a function of temperature. The data indicate that the ratios for welds A44 and B44 ranged from approximately 0.9 to 0.94. The ratios for weld A28 were lower at most temperatures, ranging from 0.83 to 0.91. The ratios for welds A28 and A44 did not vary with temperature. The ratios for weld A28 were constant from -157 to -101°C, and increased at 22°C.

The yield stress to UTS ratio provides a qualitative indication of the strain hardening capacity of the weld metals. Fig. 19 presents yield stress to UTS ratio as a function of the strain hardening exponent, n, using data compiled from various weld metal studies. The data indicate that n is inversely

proportional to the yield stress to UTS ratio. The ratios calculated in the present study are typical of high strength weld metals [Saunders, 1975] and indicate a relatively low capacity for strain hardening. The ratios also suggest that, at low temperatures, weld A28 should have a slightly higher strain hardening exponent than welds A44 and B44.

Fig. 20 shows reduction of area as a function of temperature. At temperatures ranging from 22 to -130°C, the values were equivalent for the three welds, and were insensitive to temperature. Values dropped slightly at -157°C, and showed a dramatic decrease at -196°C. Large decreases in reduction of area during low temperature tensile tests have been attributed to a transition from slip-induced to twin-induced fractur [Oates, 1968].

Cleavage Fracture Stress

The cleavage fracture stress data are presented in Table 8 and Fig. 21. The values appear to be relatively temperature independent from -101 to -157°C. This insensitivity to temperature has been associated with slip-induced fracture and said to be indicative of a propagation-controlled fracture mechanism [Knott, 1973]. At -196°C, the values decreased. A decrease in cleavage fracture stress at -196°C was seen by Bowen and Knott [1984] in A533B pressure vessel steel. Oates [1969] found that cleavage fracture stress of a manganese steel decreased with decreasing temperature. He associated the temperature dependence with the onset of twin-induced fracture. The sharp

decrease in reduction of area observed at -196°C for welds A44 and B44 supports the Oates theory, and suggest that the reduction in cleavage fracture stress at this temperature may have been caused by a transition from slip-induced to twin-induced fracture.

Welds A28 and A44 had similar cleavage fracture stress values from -101 to -157°C, indicating that weld metal cooling rate had little effect on the cleavage fracture stress. Weld B44 had lower values, indicating a detrimental effect of its composition on cleavage fracture stress.

Cleavage fracture stress measurements for high strength, martensitic steel weld metals have not been previously reported. Furthermore, the influence of cooling rate and composition has not been examined for any weld metals. Consequently, these results cannot be discussed in terms of previous findings. However, it is of interest to note that cleavage fracture stress values of C-Mn weld metals have been measured and predicted [Anelli and Buzzichelli, 1983; McRobie and Knott, 1985; Tweed and Knott, 1983]. Fig. 22 compares the data generated in the current study to the range of values reported in the literature for C-Mn weld metal. The data show that the stress levels reported in the literature are generally lower than those measured in the present study. This is due to the strength difference between the weld metals examined in the present study and those referenced from other investigations. The C-Mn weld metals investigated in the literature had ferritic structures and thus had lower yield stresses than the martensitic weld metals studied herein. The

lower yield stress of the C-Mn weld metals results in a lower available notch-root tensile stress and reduced cleavage fracture stress values.

Charpy V-notch Transition Behavior

Tables 9 through 11 present the results of Charpy V-notch (CVN) testing of welds A28, A44, and B44. Figure 23 presents absorbed energy values as a function of temperature. The percentage of shear fracture versus temperature is presented in Fig. 24. To facilitate easy comparison of the three welds, Figs. 25 and 26 present trend lines, representing the approximate average of the absorbed energy values and the lowest measured shear fracture values, respectively. The effect of cooling rate on absorbed energy can be determined from Fig. 25 by comparing the curves for welds A28 and A44. The data show that decreasing cooling rate produced increased absorbed energy levels in the upper shelf and upper transition regions. In the mid-transition and the lower shelf regions, there was no significant difference in absorbed energy levels. Fracture appearance curves, shown in Fig. 26, indicate that increasing cooling rate caused the transition from 100% shear fracture to a mixed mode of cleavage and ductile fracture to occur at a higher temperature. As was the case with the absorbed energy data, cooling rate had no significant effect on fracture appearance in the mid- and lower-transition regions.

Comparing the data shown for welds A44 and B44 illustrates the effect of the compositional differences between wires A and B

on CVN properties. Weld B44 is shown to have upper shelf energies that are significantly higher than those of weld A44. Within the transition and lower shelf regions, weld A44 generally displayed higher energy values the weld B44. In addition, the absorbed energy curve for weld B44 is shifted to higher temperatures, by approximately 20°C, compared to the curve for weld A44. A similar shift is seen in the fracture appearance curves shown in Fig. 26, indicating that weld B44 had a higher transition temperature than weld A44.

Scanning electron microscopy of specimens from the three welds indicated that fracture in the upper shelf region involved a discontinuous-shear mechanism. Figure 27 (specimens A28-41 and B44-9) shows the striated appearance of the fracture surfaces. Figure 28 presents the same fracture surfaces at a higher magnification. The striations were revealed to be alternating regions of shallow and coarse dimples that occurred in a zig-zag type pattern. This type of fracture has been noted for other martensitic microstructures [Chipperfield and Knott, 1975; Saunders, 1975; You and Knott, 1982; Gudas, 1985]. The shallow dimples reportedly result from localized shear fracture of carbide/matrix interfaces. The larger voids are thought to initiate from nonmetallic inclusions. With this fracture mode, ductile fracture resistance increases with decreasing carbide and inclusion content, decreased yield stress, and increased strain hardening capacity.

This micromechanism can be used to explain the relative upper shelf performances of the three welds. Weld B44 displayed the highest upper shelf energy due to a combination of lower carbon content, which would decrease carbide content, and lower yield stress. Weld A44 had the lowest upper shelf energy because of its carbon content, high yield stress, and low strain hardening capacity, inferred from its high yield stress to ultimate tensile stress ratio. The carbon content of weld A28 was offset by its lower yield stress and higher strain hardening capacity and resulted in intermediate upper shelf performance.

As test temperature was decreased, this ductile mechanism was replaced with increased proportions of brittle fracture. Figure 29 illustrates that brittle fracture occurred by a quasicleavage mechanism, characterized by small, ill-defined facets. The fractures showed considerable tearing between cleavage facets, giving a much more ductile appearance than standard cleavage fracture. This fracture mode is typical of high strength, tempered martensitic structures [Saunders, 1975; Gudas, 1985]. The brittle fracture mechanism was characterized further; however, discussion of this information will be deferred to a later section.

The ductile-brittle transition temperature (DBTT) and the fracture appearance transition temperature (FATT) were determined from the curves shown in Figs. 25 and 26. The DBTT was defined as the temperature at which the following energy criterion was met;

Energy = (upper shelf - lower shelf)/2 - upper shelf (22).

The FATT was defined as the temperature at which the fractured specimens displayed 50% shear fracture. Table 12 presents the DBTT and FATT for each weld.

The transition temperatures of welds A28 and A44 were approximately equal. This is consistent with the cleavage fracture stress data and indicates that cooling rate had no effect on DBTT and FATT. Previous studies of the transition behavior of high strength steel weld metals have not clearly defined the influence of cooling rate. Strunck and Stout [1972] found that increasing the cooling rate at 700°C from 16 to 110°C/s, resulted in a 30°C decrease in the 54 J transition temperature. Conversely, Dorschu and Lesnewich [1964] reported that increasing the cooling rate at 700°C from 33 to 117°C/s caused the 27 J transition temperature to increase from -101 to -84°C. Oldland [1988] reported that decreasing cooling rate caused a decrease in 50% FATT.

Comparing the data for welds A44 and B44 demonstrates that the compositional differences between these welds caused a significant variation in transition behavior. The DBTT and FATT of weld A44 were 20 and 30°C lower, respectively, than those of weld B44. This trend does not totally agree with the results of previous studies of the relationship between composition and toughness. Referring back to Table 3, weld A44 had higher carbon, chromium, and vanadium contents than weld B44. These elements are all considered to be detrimental to impact properties [Oldland, 1988]. Additionally, weld A44 had less nickel, an element added

to increase toughness, than weld B44. Only the higher manganese and lower molybdenum contents of weld A44 are consistent with its lower transition temperature [Dorschu and Lesnewich, 1964; Enis and Telford, 1968; Oldland, 1988].

The remainder of this study will attempt to explain the relative differences in the transition behavior of the three weld metals. Emphasis will be on identifying, through an analysis combining analytical and experimental findings, the microstructural features controlling ductile-brittle transition behavior. A primary focus will be to propose a mechanism that explains both the insensitivity to cooling rate and the detrimental effect of the wire B composition. It is significant that the transition temperatures and cleavage fracture stress data are in qualitative agreement, because the primary tool of the upcoming analysis is an expression that relates microstructural unit size to cleavage fracture stress. The following section addresses the critical stage of the analysis, establishing a quantitative dependence of transition temperature on cleavage fracture stress.

DEPENDENCE OF DUCTILE-BRITTLE TRANSITION BEHAVIOR ON σ_c

DBTT and FATT data indicated that cooling rate had little effect on transition behavior and that the composition of wire A was superior to that of wire B. These results show qualitative agreement with the cleavage fracture stress data, suggesting a possible correlation between σ_c and transition temperature. This section will verify this correlation by examining the quantitative

relationship between transition temperature and σ_c for the three weld metals.

The relationship between σ_c and transition temperature was described by Armstrong et al. [1988] as

$$T_c = [(ß_o - ß_1 \ln\epsilon)^{-1}][\ln(\alpha B_o) - \ln\{\sigma_c - \alpha(\sigma_G + k_y l^{-½})\}] \quad (13).$$

This expression was used to calculate transition temperatures for welds A28, A44, and B44. Table 13 summarizes the values used for each variable in Eq. 13. The values of the experimental constants $ß_o$, $ß_1$, and B_o were derived by Sandstrom and Bergstrom [1984] from C-Mn steel plate. The values for α, the stress intensification factor, and ϵ, the strain rate, were also taken from Sandstrom and Bergstrom [1984]. The term $(\sigma_G + k_y l^{-½})$, which represents the athermal component of the yield stress, was assumed to be approximately equal to the static, room temperature yield stress. Finally, lower bound estimates at a 90% confidence level, derived from the cleavage fracture stress data generated within the -101°C to -157°C temperature range, were used for σ_c. This was based on the assumption that the lower bound cleavage fracture stress for slip-induced fracture controls ductile-brittle transition. A Log-Normal statistical model was applied to estimate the lower bounds. The algorithm that was used, taken from Ang and Tang [1975], is presented in Appendix B. Log-Normal statistics were chosen based on the results of a Monte-Carlo simulation performed by Kirk [1987], which compared the accuracy of lower bound estimates made using Normal, Weibull, and Log-Normal statistical models. He concluded that, for cases in which: (1) the

statistical distribution of the quantity being sampled is unknown; and (2) the sample size is between 3 and 31, lower bound estimates made using Log-normal statistics are generally more accurate than those made using Normal and Weibull statistics.

The calculated transition temperatures are presented in Table 14, along with the transition temperatures measured from the CVN transition curves. The calculated values for welds A44 and B44 showed excellent agreement with the measured FATT values. Conversely, the calculated value for weld A28 was significantly lower than the measured transition temperatures. Three major reasons for the discrepancy are suggested:

(1) There may be significant error associated with the estimating lower bound value of σ_c from six data points.

(2) Because the experimental constants used were derived from C-Mn steel plate, the analysis may not accurately express the temperature and strain rate dependence of the yield stress. Moreover, the static, room temperature yield stress may not closely approximate the athermal component of yield stress at ϵ=400s^{-1}.

(3) The transition temperature analysis may not adequately address the appropriate metallurgical/mechanical properties.

While there is undoubtedly some error associated with both the yield stress and lower bound σ_c estimates, this error is inherent to the analysis, and therefore would be expected to result in significant discrepancies between the calculated and measured values for all of the welds. The agreement for welds A44

and B44; however, was excellent. A large discrepancy occurred only for weld A28, suggesting that a metallurgical or mechanical property difference existed between it and welds A44 and B44 that was not addressed by the model. A possible deficiency of the model is that it does not account for differences in strain hardening behavior. Knott [1966] reported that, at temperatures above the general yield temperature, attainment of the critical cleavage fracture stress could be attributed to a strain hardening-induced increase in the flow stress. The ductile-brittle transition criterion, Eq. 8, modified to accommodate this, can be written as

$$\sigma_c = \alpha(\sigma_y + \Delta\sigma) \tag{23}$$

where $\Delta\sigma$ is a function of strain [Knott, 1973], and thus of the strain hardening exponent. The yield stress to ultimate tensile stress ratios for welds A44 and B44 were very high, indicating low strain hardening capacity, and a low value for $\Delta\sigma$. The ratio for weld A28 was somewhat lower, indicating a higher strain hardening exponent than welds A44 and B44 and a greater value for $\Delta\sigma$. Therefore, it is proposed that, due to strain hardening, the flow stress at the notch tip of the specimens tested from weld A28 was higher than the yield stress component calculated from Eq. 13. This resulted in a measured transition temperature that was higher than the calculated value. This effect was not as great for welds A44 and B44 because of their lower strain hardening capacities. This argument should be examined in detail in future work.

In general, this analysis appears to predict the transition behavior reasonably well. The predicted values for welds A44 and B44 displayed excellent agreement with measured values. Furthermore, the analysis correctly predicted that wire A produced weld metal with a lower transition temperature than wire B. Although the effect of cooling rate was not accurately reproduced, the postulated source of error does not refute the validity of the analysis for these weld metals.

These results provide quantitative verification of the dependence of ductile-brittle transition behavior on σ_c. Thus, the relative performances of the weld metals can be explained in terms of their respective σ_c properties. This reduces the problem of identifying the factors controlling ductile-brittle transition to a determination of the microstructural features that control σ_c. Recalling the introductory review of the critical tensile stress criterion, this can be accomplished in two stages. The first involves calculation of critical microcrack sizes using Griffith-type models. These calculated sizes can then be correlated to specific microstructural features present in the material. The following section presents such an analysis for welds A28, A44, and B44.

MICROSTRUCTURAL FEATURES THAT CONTROL DUCTILE-BRITTLE TRANSITION

As stated earlier, a widely accepted micromechanism for brittle fracture involves initiation of a microcrack at some microstructural feature which cracks under the influence of dislocation arrays [Bowen and Knott, 1984]. The critical stage in

growth-controlled fracture is propagation of this microcrack into the matrix. The cleavage fracture stress represents the critical level of stress for propagation. This critical cleavage fracture stress criterion was expressed by Curry and Knott [1978], as a modified form of the Griffith-Orowan equation;

$$\sigma_c = [2\pi E\gamma_p/2(1-\nu^2)a]^{\frac{1}{2}}, \text{ penny-shaped crack} \quad (4)$$

$$\sigma_c = [4E\gamma_p/\pi(1-\nu^2)a]^{\frac{1}{2}}, \text{ through-thickness crack} \quad (5)$$

where σ_c is the cleavage fracture stress, a is the critical microcrack size, E is Young's modulus, ν is Poisson's ratio, and γ_p a plastic work term. This expression illustrates that σ_c is inversely proportional to the critical microcrack size.

Rearranging Eqs. 4 and 5 gives the expressions for critical crack size;

$$a = \pi E\gamma_p/(1-\nu^2)\sigma_c^2, \text{ penny-shaped crack} \quad (6)$$

$$a = 4E\gamma_p/\pi(1-\nu^2)\sigma_c^2, \text{ through-thickness crack} \quad (7).$$

Assuming E = 206 MPa, ν=0.3, γ_p=14 Jm^{-2} [Knott, 1977], and using the Log-normal, lower bound σ_c values presented in Table 13, Eqs. 6 and 7 were solved for welds A28, A44, and B44. Table 15 presents the critical microcrack crack sizes predicted from this analysis. Predicted sizes for penny-shaped cracks varied from 1.38μm to 1.62μm; predicted sizes for through-thickness cracks varied from 0.56μm to 0.66μm.

Previous studies have demonstrated that predicted crack sizes correspond well with the size of the microstructural features controlling brittle fracture [Low, 1954; Brozzo et al., 1977; Curry and Knott, 1979; Bowen and Knott, 1984]. The

microstructural features found in the weld metals examined in the present study include prior austenite grains, martensite or bainite packets, carbides, and nonmetallic inclusions [Chen et al., 1978; Oldland, 1988]. Table 5 showed that the prior austenite grain sizes in the notch root region varied from 36μm to 42μm. These sizes are one to two orders of magnitude greater than the calculated crack sizes. In addition, under prior austenite grain size control, toughness properties would be inversely proportional to the prior austenite grain sizes. However, as shown in Table 5, the prior austenite grain size of weld B44 was less than that of weld A28. This is not consistent with the lower σ_c values and higher transition temperature displayed by weld B44, eliminating prior austenite grain size as the controlling feature.

A qualitative indication of the lath packet sizes can be obtained from Figs. 10 through 15. Assuming that major orientation changes occur at packet boundaries, the largest packets appear to be significantly greater than the calculated microcrack sizes. Oldland [1988] also presented martensite and bainite lath packets for high strength weld metals. No sizes were reported, but examination of the published micrographs indicated that the largest packets were much greater than the microcrack sizes calculated in the present study. Bowen and Knott [1984] found, for A533B pressure vessel steel, that packet size is on the order of one-third the size of the prior austenite grain. Furthermore, they noted that packet size is strongly dependent on prior austenite grain size. Assuming the same strong dependence

for welds A28, A44, and B44, and recalling the inability of prior austenite grain size differences to explain the toughness observations, lath packet size can also be eliminated as the controlling feature.

Carbide distribution has been shown to control fracture properties in many steels [Gudas, 1985]. Deb et al. [1987] reported a carbide size of approximately 0.025μm for a similar Ni-Cr-Mo-V weld metal with a predominantly martensitic structure. This carbide size is one to two orders of magnitude less than the calculated microcrack sizes. Assuming a similar carbide size distribution for the welds A28, A44, and B44 suggests that carbides are not the microstructural features controlling transition behavior. In addition to the size discrepancy, welds A28 and A44 had higher carbon, chromium, and vanadium contents than weld B44. Increases in these elements would tend to increase carbide size and content. Additionally, weld A28 was cooled at a slower rate than weld B44, and thus had more time for coarsening of carbides during tempering. These points imply that welds A28 and A44 should have a greater carbide content and size, and thus a lower σ_c and higher transition temperature, than weld B44. This is not consistent with the experimental or analytical results.

The trends displayed by the σ_c data and the calculated crack sizes point to nonmetallic inclusions as the controlling feature. The calculated crack size range is comparable to nonmetallic inclusion diameters reported by Ramsey et al. [1989] for weld metals with compositions very similar to those examined

herein. Moreover, little variation in inclusion size would be expected with cooling rate, which is consistent with the minimal influence of cooling rate on σ_c and transition temperature. The lower σ_c values and higher transition temperature of weld B44 is consistent with its higher calculated titanium oxide content.

Fracture surfaces of the notched bend specimens were examined, using scanning electron microscopy, to determine whether inclusions could be identified at cleavage initiation sites. The sites for brittle fracture initiation were determined by tracing river patterns. The examinations indicated, primarily with specimens from weld B44, that inclusions on the order of 0.5 to 1.0μm, were observed at fracture initiation sites. Many of the inclusions appeared to have cracked, probably due to the influence of dislocation pile-ups. The initiation areas were generally associated with large flat facets. Figures 30 and 31 illustrate examples of inclusion-initiated fracture in welds A44 and B44.

Energy dispersive x-ray analyses were performed on the initiating inclusion shown in Fig. 31 and on the matrix adjacent to the inclusion. This was intended to distinguish the composition of the inclusions from that of the matrix. Results revealed that the inclusion displayed a much stronger titanium peak than that observed in the matrix spectrum, indicating that this was a titanium-bearing nonmetallic inclusion. The x-ray spectrum of the inclusion is shown in Fig. 32.

Table 3 showed that weld B44 contained 0.010% titanium, compared to 0.006% for welds A28 and A44. As indicated in

Table 4, this suggests that weld B44 should have the highest titanium oxide content. Peters [1989] measured the influence of titanium content on the inclusion distribution of high strength steel weld metal. Results indicated that both average inclusion size and volume fraction increased with increasing titanium. In Peters' work, an increase in titanium content of 0.004%, the difference between weld B44 and welds A28 and A44, resulted in an increase in average inclusion size of approximately 0.05μm. This correlates reasonably well with the differences in the calculated microcrack sizes of the three welds.

The results of this study suggest that the transition behavior of the high strength, martensitic weld metals examined herein depends critically on nonmetallic inclusion content. The increased transition temperature shown by weld B44 may be attributed to a reduced σ_c, caused by coarse, titanium-bearing inclusions. The higher titanium content of weld B44, in comparison to welds A28 and A44, is consistent with a larger inclusion size. Welds A28 and A44 had comparable titanium and oxygen contents, but were produced at different cooling rates. The similarity in the transition temperatures of these welds can be explained by their similar compositions and the minimal effect of cooling rate on inclusion size.

This inclusion-controlled mechanism is a tentative proposal, and requires additional microstructural and fractographic evidence. However, it is in good agreement with the literature. Several authors have reported inclusion-initiated cleavage

fracture in COD and CVN specimens removed from ferritic steel weld metals [Tweed and Knott, 1983, 1987; McRobie and Knott, 1985; Zhang et al., 1986; Chen and Yan, 1988]. In addition, this theory is consistent with inclusion-controlled cleavage fracture mechanisms proposed by Tweed and Knott [1983] for C-Mn weld metals and by Bowen and Knott [1984] for A533B steel in the martensitic condition.

It should be noted that previous studies have identified lath packet size as the controlling feature for martensitic and bainitic steels and weld metal [Naylor, 1979; Hagiwara and Knott, 1981; Oldland, 1988]. These proposals are generally based on: (1) fractographic observations demonstrating a correlation between fracture facet size and packet size; and (2) a trend of increasing toughness with decreasing packet size. The first observation is expected, since the only large angle deviations occur at packet boundaries. Lath boundaries have small angle deviations and thus would not be expected to change fracture path considerably. As for the second observation, fractographic observations show that crack propagation through a packet is largely unperturbed, until a packet boundary is met. Therefore, for over a given propagation distance, it follows that less energy would be required to propagate a crack across large packets than smaller packets. As stated by Bowen and Knott [1984], these observations explain the influence of packet size on the resistance to propagation, but do not establish propagation of a packet-sized microcrack as a prelude to macroscopic cleavage fracture.

An additional contribution of packet size may relate to dislocation pile-ups. Increased packet size increases the effective grain size. This would tend to increase dislocation pile-up stresses, favoring microcrack nucleation [Tweed and Knott, 1983]. The location of initiating particles in regions of coarse cleavage facets (Figs. 31 and 32) supports this theory and suggests that packet size, as well as inclusion population, contributes to transition performance.

SUMMARY AND CONCLUSIONS

The objective of this study was to determine the microstructural features that control the ductile-brittle transition behavior of high strength steel weld metals with predominantly martensitic microstructures. Three weld metals were produced using two filler wires, designated wires A and B, and at two cooling rates, 28°C/s and 44°C/s. Wire A was used to produce both a high and low cooling rate weld metal; wire B was used to produce a high cooling rate weld metal only. The filler wire/cooling rate combinations were designed to (1) produce microstructures with a high percentage of martensite, and (2) isolate the influence of cooling rate and composition. Tensile, CVN, and cleavage fracture stress (σ_c) tests, as well as chemical metallographic, and fractographic analyses were performed on each weld metal.

The tensile data indicated that yield stress decreased with decreasing cooling rate. This was attributed to the increased

tempering and associated softening that accompanies slower cooling rates. At the same nominal cooling rate, wire A displayed a higher yield stress than wire B. This was attributed primarily to the higher carbon, chromium, and vanadium contents of wire A.

The σ_c values were largely temperature insensitive over the range of -101 to -157°C, supporting a tensile stress-controlled, slip-induced cleavage fracture mechanism. The values decreased at -196°C, indicating that a transition from slip-induced to twin-induced fracture occurred at this temperature.

Results of CVN tests indicated that cooling rate had little effect on transition behavior and that the transition behavior wire A was superior to that of wire B. Similarly, the σ_c of wire A was superior to that of wire B, and σ_c was largely insensitive to cooling rate.

From σ_c measurements and static yield stress data, corrected for strain rate and for local stress elevations associated with the notch, CVN transition temperatures were derived analytically. Results indicated that the calculated transition temperatures showed fairly good agreement with measured CVN 50% fracture appearance transition temperatures (FATT). The good correlation between the calculated and measured values verified a quantitative dependence of 50% FATT on σ_c. Following this, the size of the cleavage-nucleating microcracks were calculated from a modified Griffith-Orowan expression. Results indicated that the microcrack size ranged from approximately 0.5 to 1.5μm. These sizes are typical of weld metal inclusions. Fractographic analyses of

tested notched bend specimens revealed that titanium-bearing inclusions, approximately 0.5 to 1.0μm in diameter, were directly associated with cleavage initiation.

These results suggest that ductile-brittle transition behavior in these high strength, martensitic weld metals is controlled by inclusion population. The higher transition temperature shown by the wire B weld metal appears to be due to its higher titanium content and the concomitant presence of coarse, titanium-bearing inclusions. The similar transition behavior of the two wire A weld metals was apparently due to their similar compositions and the minimal effect of cooling rate on inclusion size.

The following conclusions can be drawn from this study:

1. The σ_c of high strength, martensitic steel weld metals is largely temperature-independent from -101°C to -157°C, supporting a tensile stress-controlled, slip-induced, cleavage fracture mechanism. At -196°C, σ_c decreases, indicating that a transition to twin-induced fracture occurs at this temperature.

2. CVN transition temperatures for these weld metals can be predicted reasonably well from σ_c measurements, using an expression developed by Armstrong et al. [1988]. Improved accuracy may be achieved by incorporating strain hardening capacity in the expression. The agreement between the measured and analytical values quantitatively demonstrates the dependence of transition temperature on cleavage fracture stress for high

strength steel weld metals with predominantly martensitic microstructures.

3. For the conditions examined in this study, both the CVN transition temperature and the σ_c of high strength, martensitic steel weld metals are influenced by composition, but are relatively insensitive to cooling rate.

4. Cleavage fracture initiation in these weld metals is often associated with titanium-bearing, nonmetallic inclusions.

5. The observed CVN transition behavior, σ_c data, and fractographic observations are consistent with an inclusion-controlled mechanism. These results suggest that the transition behavior of high strength steel weld metals with predominantly martensitic microstructures depends critically on inclusion distribution. This is a tentative proposal, and requires additional microstructural and fractographic validation.

Table 1. Compositions of base material and welding wires.

Material	Composition, weight percent										
	C	Mn	Si	P	S	Ni	Mo	Cr	Cu	V	Ti
Plate	0.110	0.69	0.23	0.004	0.006	4.14	0.33	0.53	0.19	0.083	0.001
Wire A	0.093	1.71	0.24	0.006	0.004	2.10	0.63	1.02	0.047	0.010	0.010
Wire B	0.076	1.55	0.39	0.004	0.002	2.47	0.80	0.73	0.031	0.003	0.016

Table 2. Welding conditions used to fabricate welds A28, A44, and B44.

Weld ID	Wire	Heat Input (MJ/m)	Voltage (volts)	Current (amps)	Travel Speed (mm/sec)	Preheat/ Interpass Temp (^{o}C)	Cooling Rate (^{o}C/s)
A28	A	1.6	27	340	5.9	149	28
A44	A	1.2	27	340	7.6	79	44
B44	B	1.2	27	340	7.6	79	44

Table 3. Weld metal compositions and calculated carbon equivalents for welds A28, A44, and B44.

Weld ID	Composition, weight percent													
	C	Mn	Si	P	S	Ni	Mo	Cr	Cu	V	Ti	Al	O	CE
A28	0.083	1.64	0.30	0.006	0.007	2.24	0.64	1.03	0.053	0.014	0.006	0.002	0.020	0.85
A44	0.076	1.66	0.28	0.004	0.007	2.10	0.63	1.01	0.047	0.011	0.006	0.002	0.022	0.83
B44	0.066	1.46	0.35	0.007	0.003	2.40	0.83	0.70	0.041	0.004	0.010	0.003	0.022	0.78

Table 4. Inclusion contents calculated from the compositions of welds A28, A44, and B44.

Weld ID	Calculated volume percent			
	MnS	Al_2O_3	TiO_2	$MnSiO_2$
A28	0.037	0.008	0.022	0.091
A44	0.037	0.008	0.022	0.104
B44	0.016	0.012	0.037	0.081

Table 5. Prior austenite grains sizes from last-bead and reheated regions of welds A28, A44, and B44.

Weld ID	Grain size, μm	
	Last-bead	Reheated
A28	42	38
A44	36	42
B44	39	40

Table 6. Diamond pyramid hardness measurements from last-bead and reheated regions of welds A28, A44, and B44.

Weld ID	Diamond Pyramid Hardness	
	Last-bead	Reheated
A28	379	367
A44	405	361
B44	376	355

Table 7. Tensile properties of welds A28, A44, and B44.

Weld ID	Test Temp (°C)	0.2% Yield Stress (MPa)	Ultimate Tensile Stress (MPa)	Reduction of Area (%)
A28	22	994	1091	65
	22	992	1081	63
	-101	1021	1207	58
	-101	1028	1207	60
	-129	1083	1241	58
	-129	1076	1255	57
	-157	1097	1331	49
A44	22	1041	1138	60
	22	1069	1145	62
	-101	1117	1241	57
	-101	1103	1228	57
	-129	1131	1248	61
	-129	1131	1255	62
	-157	1214	1338	56
	-196	1331	1434	16
	-196	1359	1462	17
B44	22	1007	1083	62
	22	993	1069	62
	-101	1055	1172	59
	-129	1083	1200	59
	-196	1262	1386	20

Table 8. Cleavage fracture stress properties of welds A28, A44, and B44.

Weld ID	Cleavage fracture stress, MPa Test temperature, °C -196	-157	-127	-101
A28	--	2741	2850	2632
	--	2752	2817	2703
A44	2663	--	2748	2694
	2501	2889	2839	2838
B44	2612	2695	2555	2754
	2335	2449	2707	--

Table 9. Charpy V-notch properties of weld A28.

Test Temperature (°C)	Absorbed Energy (J)	Shear Fracture (%)
-118	18	10
-118	11	10
-118	16	10
-84	23	20
-84	18	20
-84	28	30
-68	54	40
-68	34	30
-68	46	40
-51	60	60
-51	56	50
-51	64	50
-34	87	100
-34	69	70
-18	80	80
-18	75	90
-18	77	100
21	77	100
21	69	100
21	77	100
66	94	100
66	77	100

Table 10. Charpy V-notch properties of weld A44.

Test Temperature (°C)	Absorbed Energy (J)	Shear Fracture (%)
-118	15	20
-118	22	10
-118	20	10
-84	18	30
-84	33	40
-84	27	40
-68	43	40
-68	41	50
-51	61	70
-51	52	70
-51	58	80
-34	65	70
-34	50	90
-34	49	90
-18	62	80
-13	62	90
-18	65	80
-1	66	90
-1	68	80
21	69	90
21	72	90
21	69	90
66	69	100
66	73	100

Table 11. Charpy V-notch properties of weld B44.

Test Temperature (°C)	Absorbed Energy (J)	Shear Fracture (%)
-118	15	10
-118	15	10
-84	22	10
-84	27	20
-84	33	30
-68	37	30
-68	27	30
-51	53	40
-51	43	30
-51	34	30
-34	65	60
-18	76	80
-18	77	60
-18	66	80
-1	95	70
-1	81	80
21	90	90
21	84	80
21	100	100
49	91	100
49	94	100
66	95	100
66	77	100

Table 12. Transition temperatures determined from CVN absorbed energy and fracture appearance data.

Weld ID	Transition Temperature, °C DBTT	FATT
A28	≈-65	≈-50
A44	≈-65	≈-50
B44	≈-45	≈-20

Table 13. Values used for each variable of Eq. 13.

Eq. 13: $T_C = [(\beta_0 - \beta_1 \ln\epsilon)^{-1}][\ln(\alpha B_0) - \ln\{\sigma_C - \alpha(\sigma_G + k_y l^{-\frac{1}{2}})\}]$

Variable	Weld A28	Weld A44	Weld B44	Comments
β_0, $^oK^{-1}$	0.0075	0.0075	0.0075	From Armstrong et al. [1988]
β_1, $^oK^{-1}$	0.0004	0.0004	0.0004	From Armstrong et al. [1988]
B_0, MPa	1000	1000	1000	From Armstrong et al. [1988]
α	1.94	1.94	1.94	From Sandstrom and Bergstrom [1984]
ϵ, s^{-1}	400	400	400	From Sandstrom and Bergstrom [1984]
$(\sigma_G + k_y l^{-\frac{1}{2}})$, MPa	993	1055	1000	Static rm temp yield stress
σ_C, MPa	2635	2682	2477	90% log normal lower bound of values within -101 to -157^oC temperature range

Table 14. Comparison of calculated and measured transition temperatures of welds A28, A44, and B44.

Weld ID	Transition temperatures, °C Calculated	Measured DBTT	Measured FATT
A28	-75	≈-65	≈-50
A44	-54	≈-65	≈-50
B44	-21	≈-45	≈-20

Table 15. Critical microcrack sizes calculated from lower bound cleavage fracture stress values.

Weld ID	Predicted micrcrack size, μm Penny-shaped	Through-thickness
A28	1.43	0.58
A44	1.38	0.56
B44	1.62	0.66

(a) Local stress causes impingement of a dislocation array on a second phase particle.

(b) The particle cracks under the influence of the dislocation pile-up stress, forming a microcrack.

(c) Macroscopic cleavage occurs when a level of tensile stress is reached that causes the microcrack to propagate into ferrite matrix.

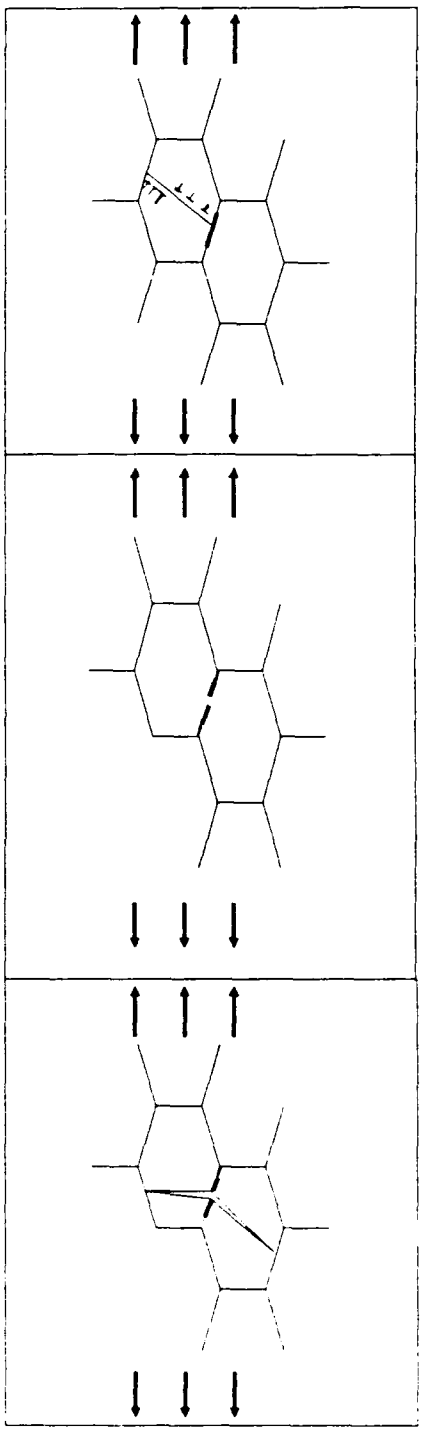

Fig. 1. Schematic illustration of cleavage fracture mechanism.

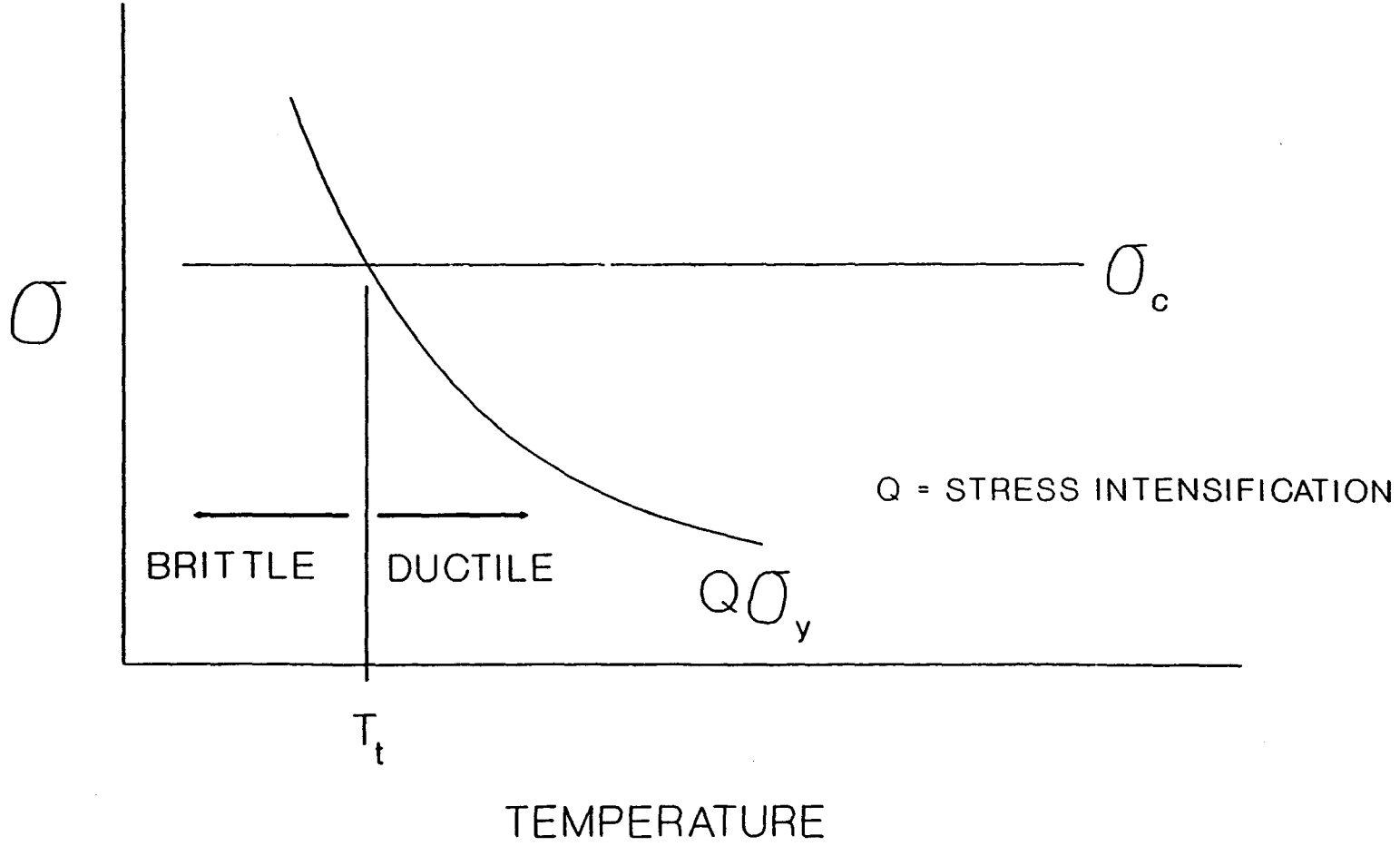

Fig. 2. Orowan [1945] theory of brittle fracture.

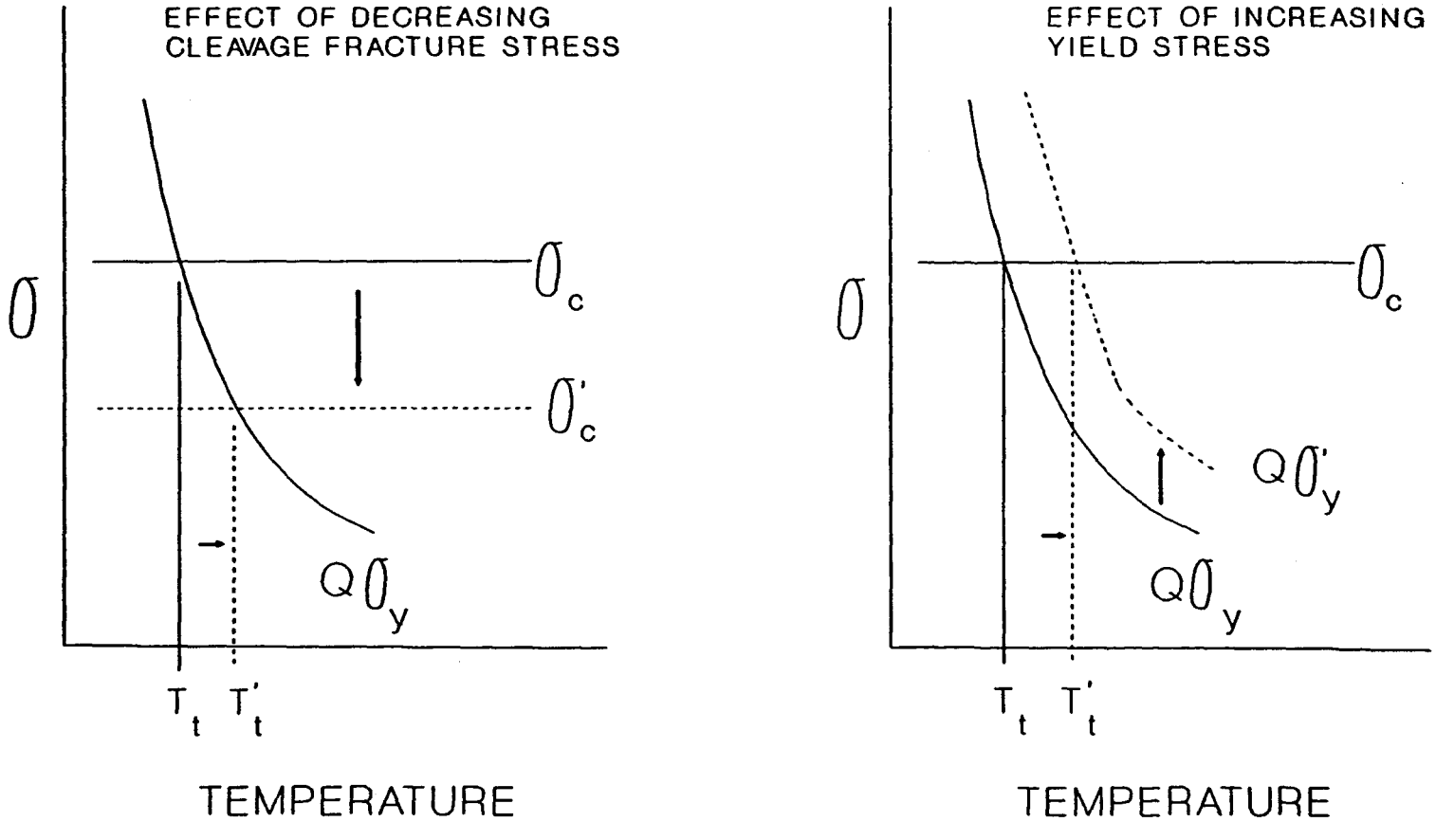

Fig. 3. Influence of σ_c and σ_y on transition temperature, T_t.

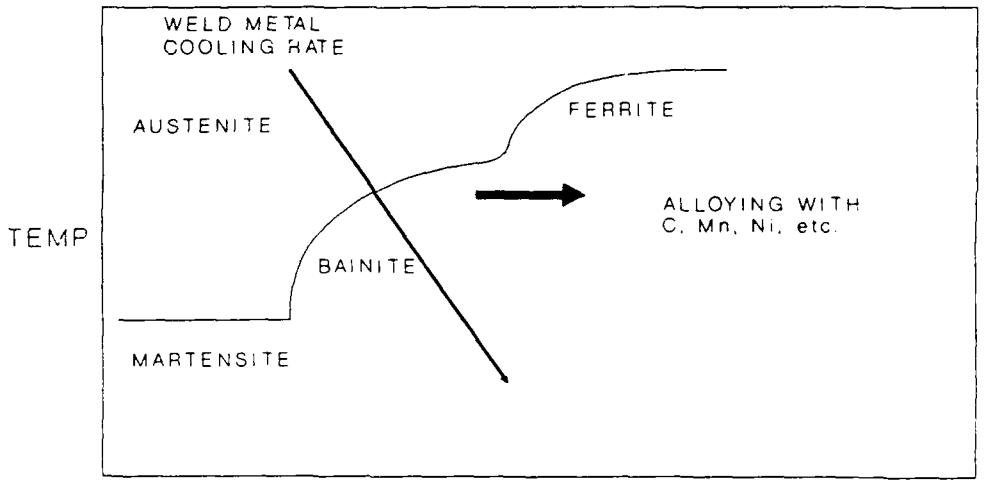

(a) Influence of alloying on transformation.

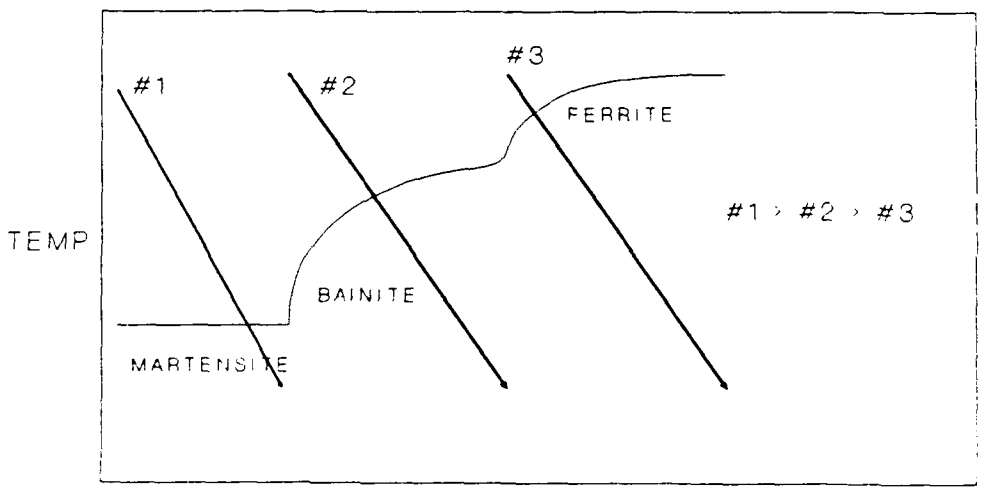

(b) Influence of cooling rate on transformation.

Fig. 4. Schematic continuous cooling transformation diagrams showing the influence of composition and cooling rate on microstructure.

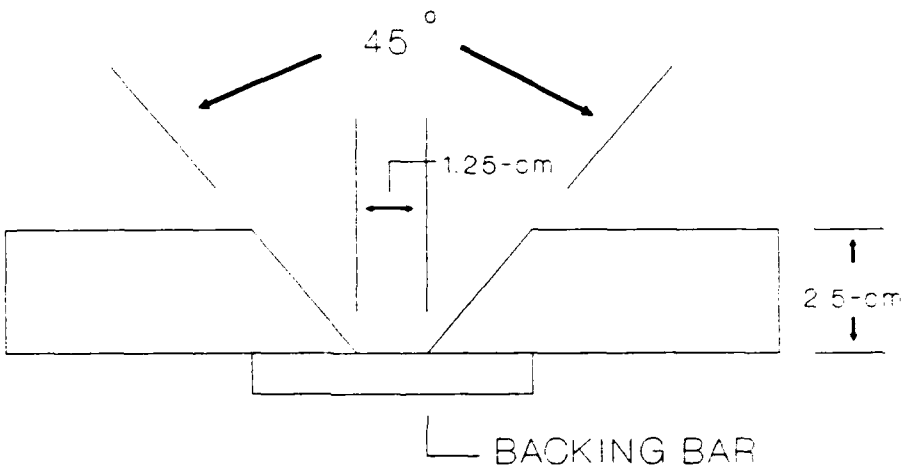

Fig. 5. Joint design.

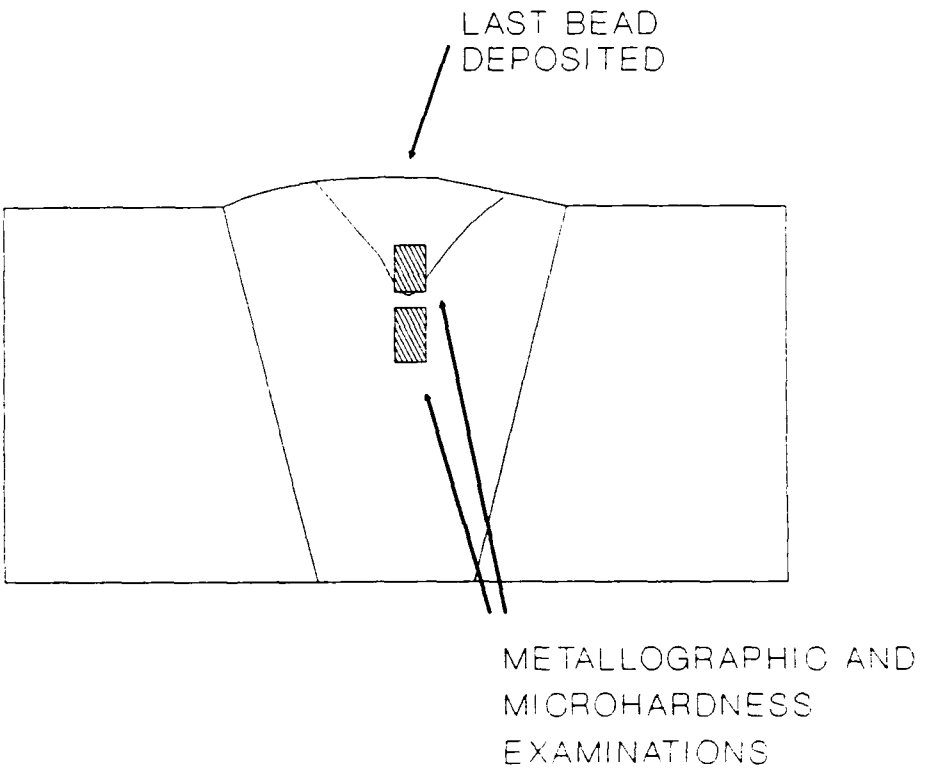

Fig. 6. Location of microstructural and microhardness examinations.

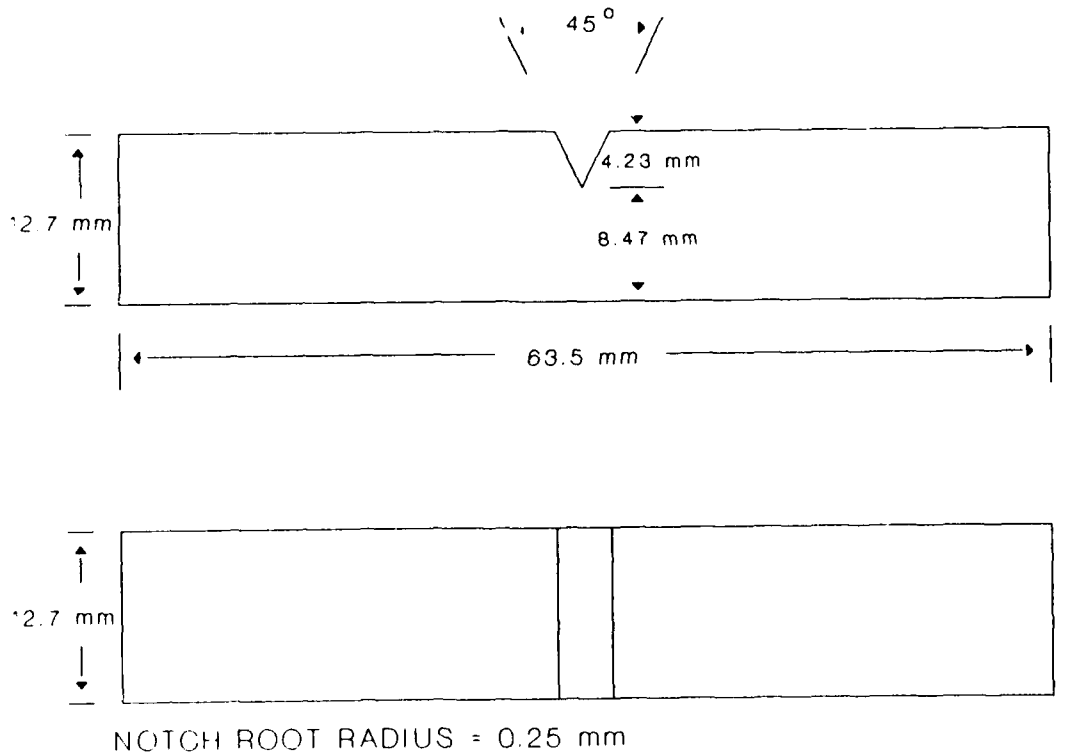

Fig. 7. Bend specimen used to measure cleavage fracture stress.

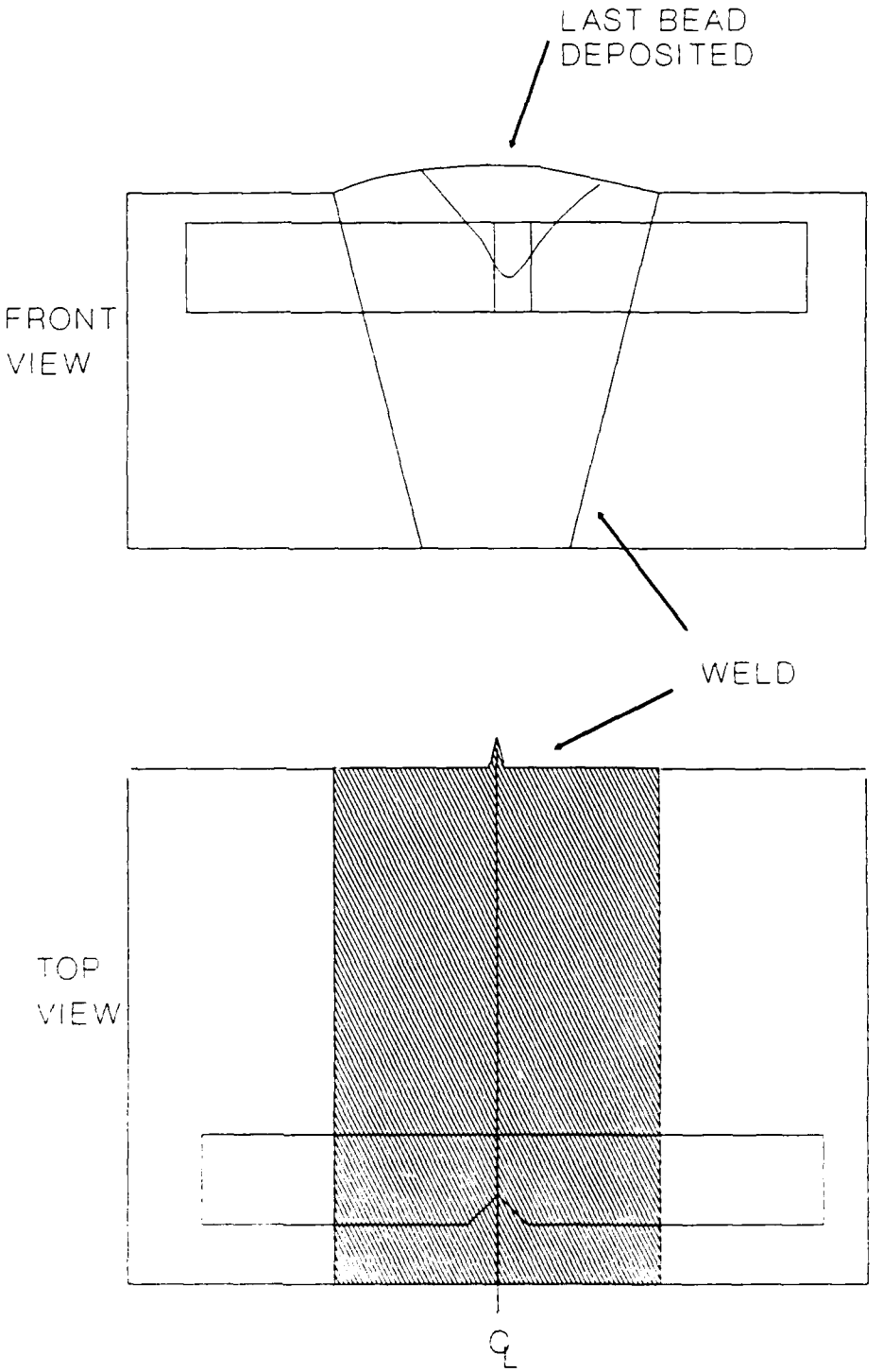

Fig. 8. Location of bend and CVN specimen removal.

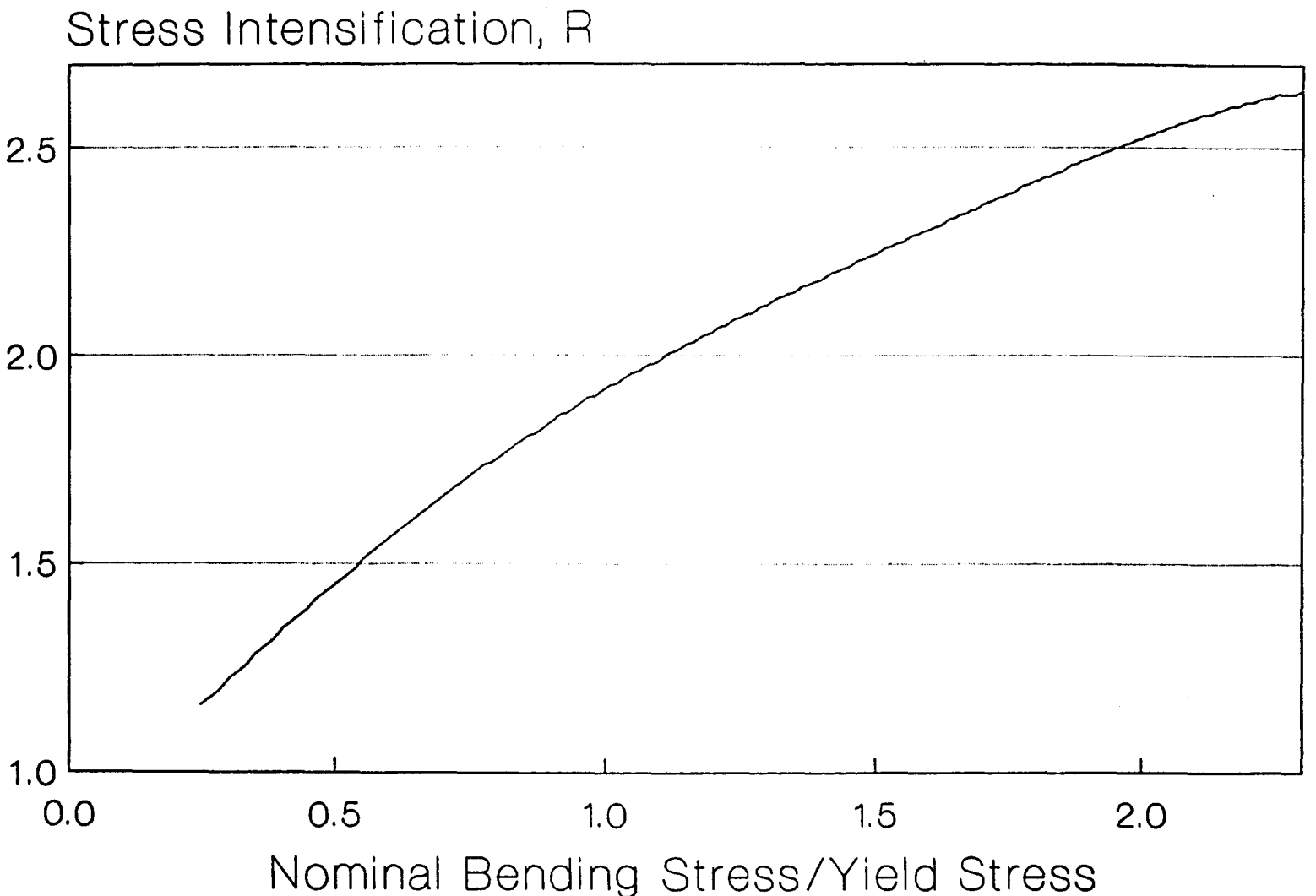

Fig. 9. Variation of stress intensification, R, with $\sigma_{nom}/\sigma_{max}$ for notched bend specimens used in this study [Griffiths and Owen, 1971].

10μm

Fig. 10. Microstructure of last-bead region of weld A28.

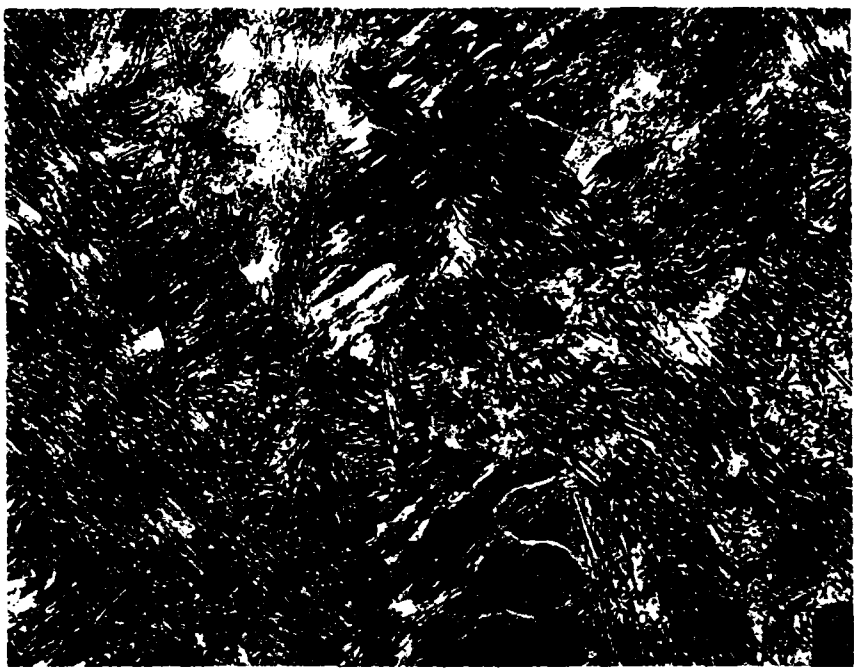

10μm

Fig. 11. Microstructure of last-bead region of weld A44.

10μm

Fig. 12. Microstructure of last-bead region of weld B44.

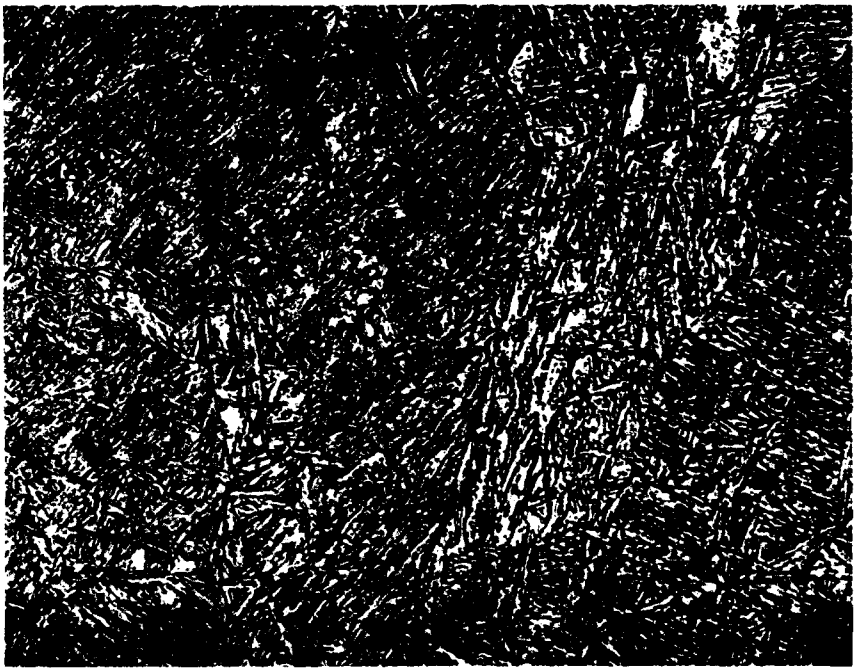

10μm

Fig. 13. Microstructure of reheated region of weld A28.

10μm

Fig. 14. Microstructure of reheated region of weld A44.

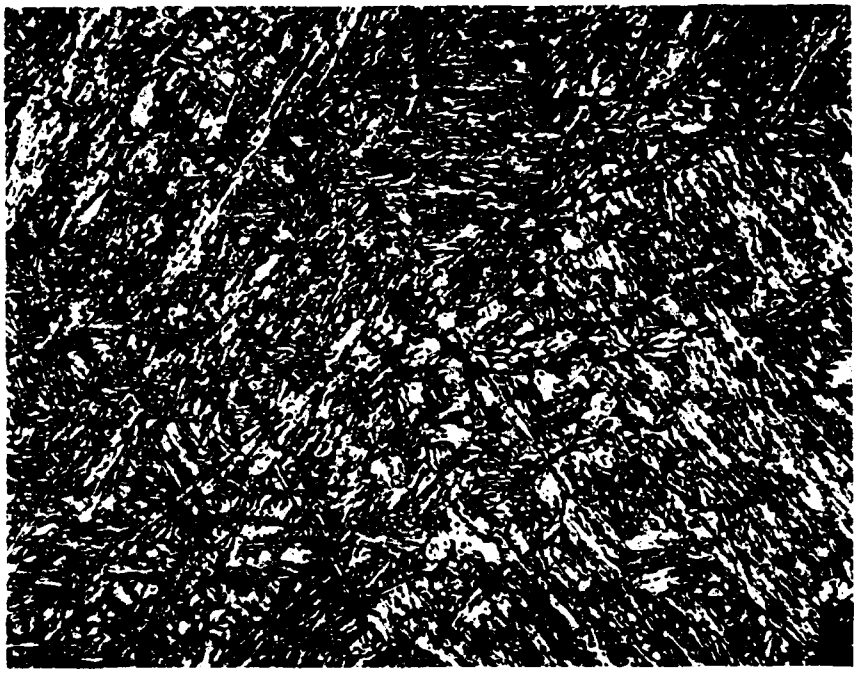

10μm

Fig. 15. Microstructure of reheated region of weld B44.

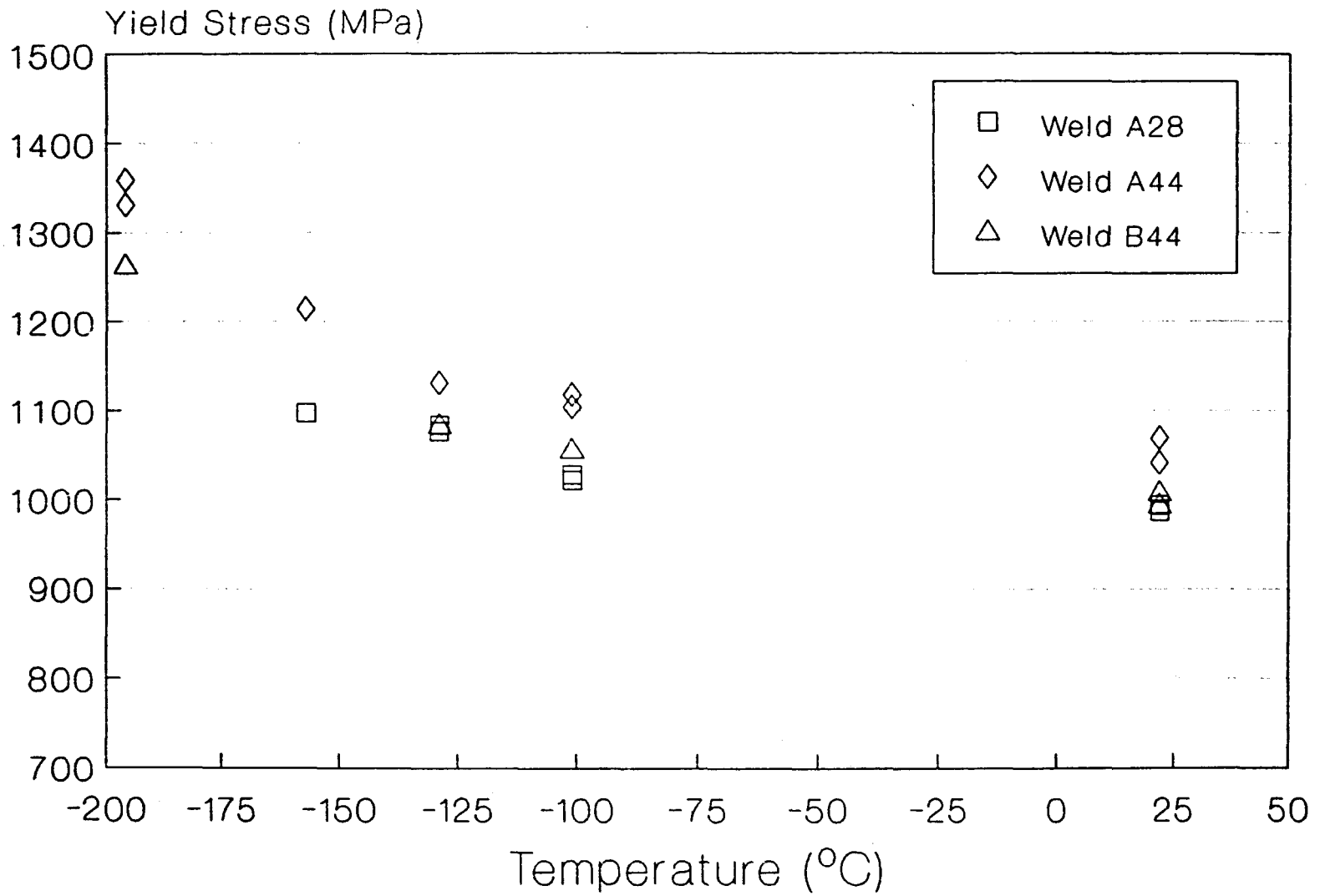

Fig. 16. Yield stress as a function of temperature for welds A28, A44, and B44.

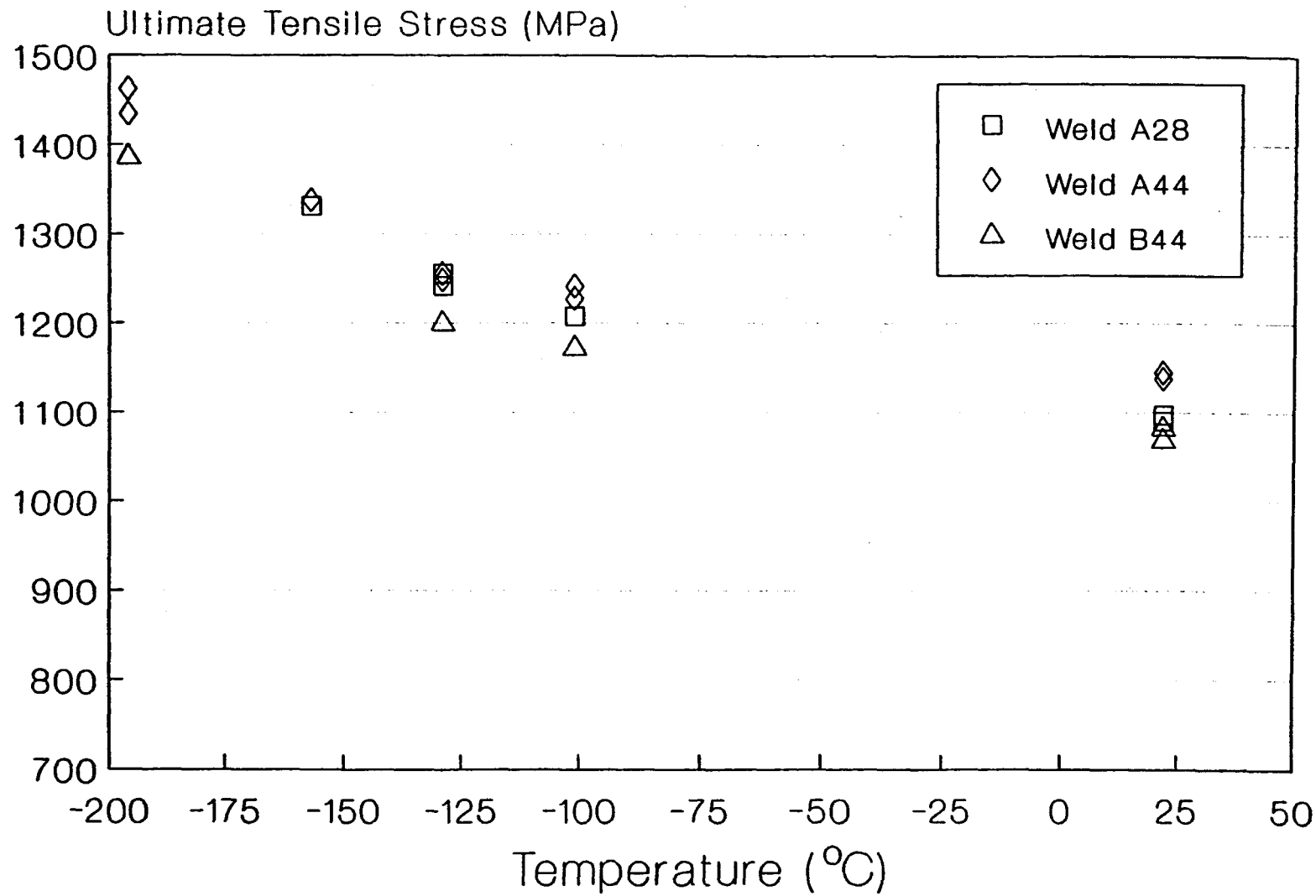

Fig. 17. Ultimate tensile stress versus temperature for welds A28, A44, and B44.

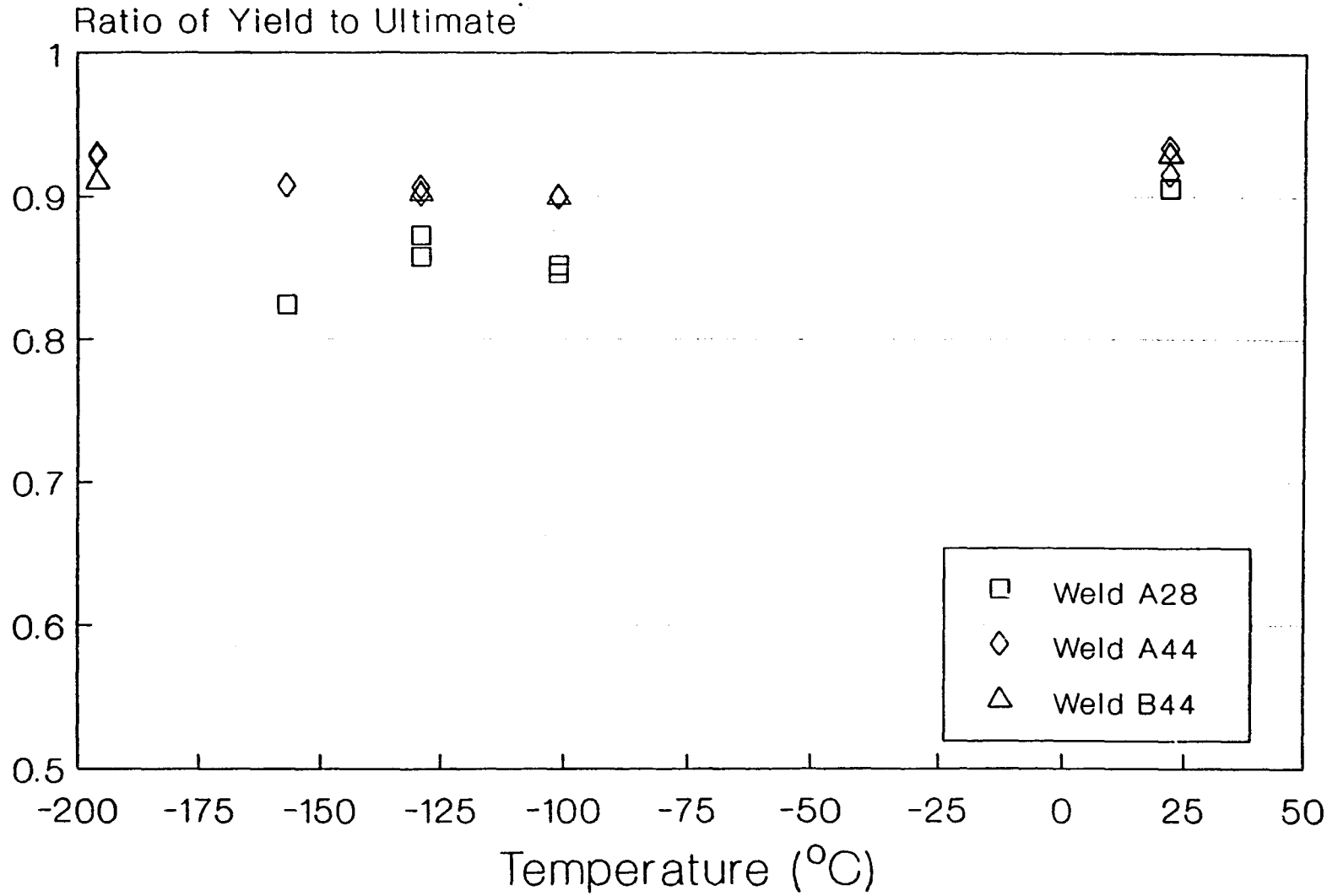

Fig. 18. Ratio of yield stress to ultimate tensile stress as a function of temperature for welds A28, A44, and B44.

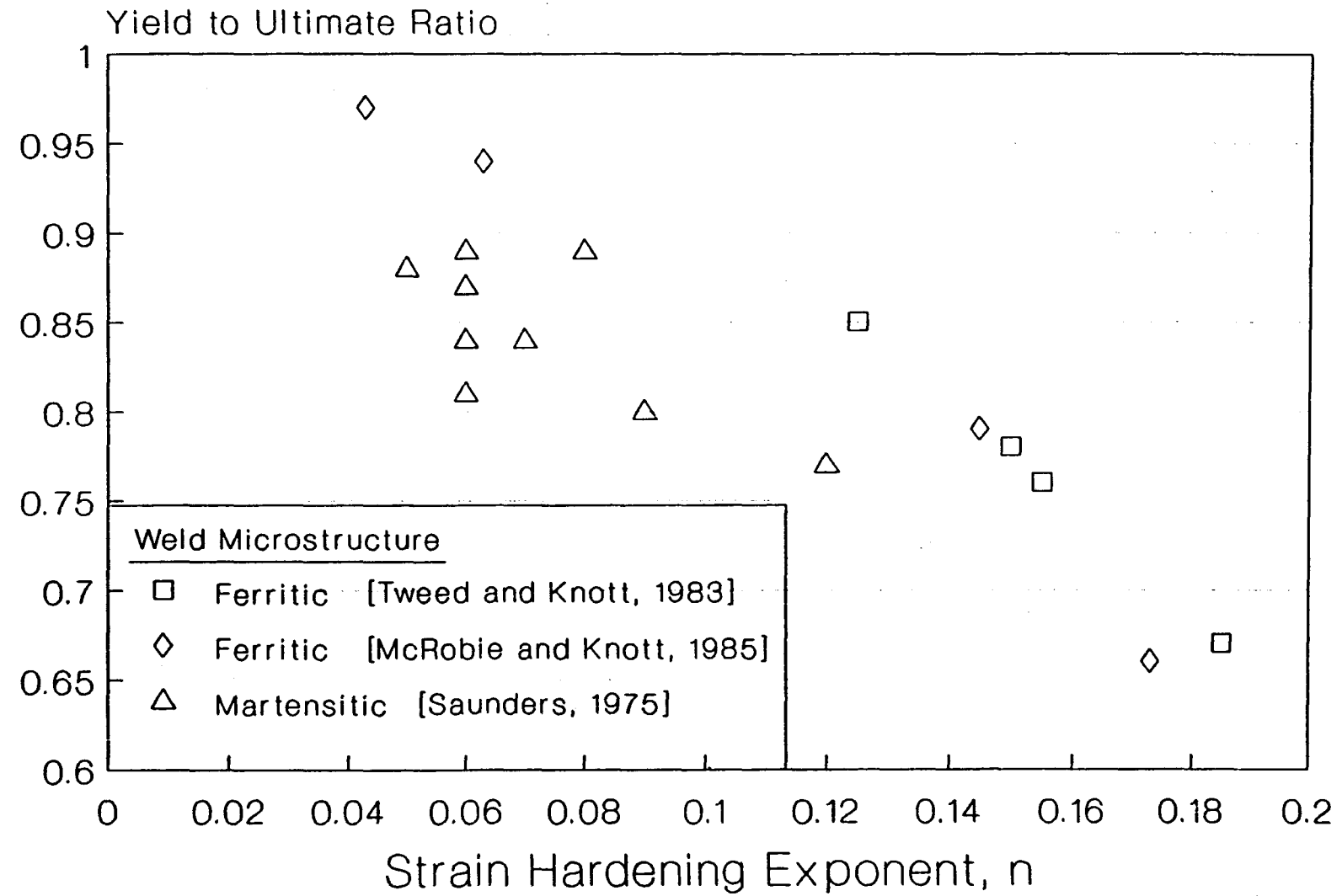

Fig. 19. Relationship between yield stress to ultimate tensile stress ratio and strain hardening exponent, n.

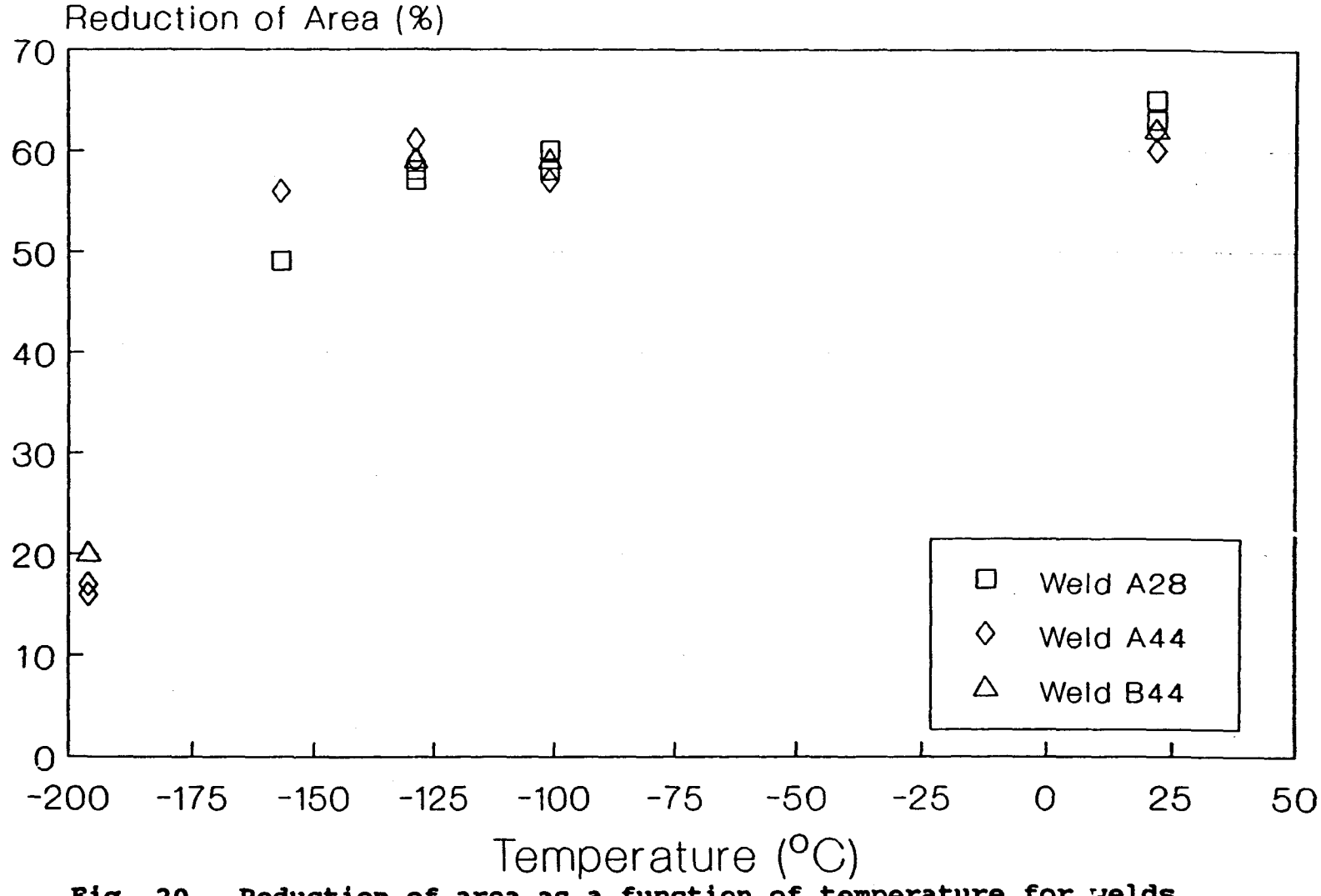

Fig. 20. Reduction of area as a function of temperature for welds A28, A44, and B44.

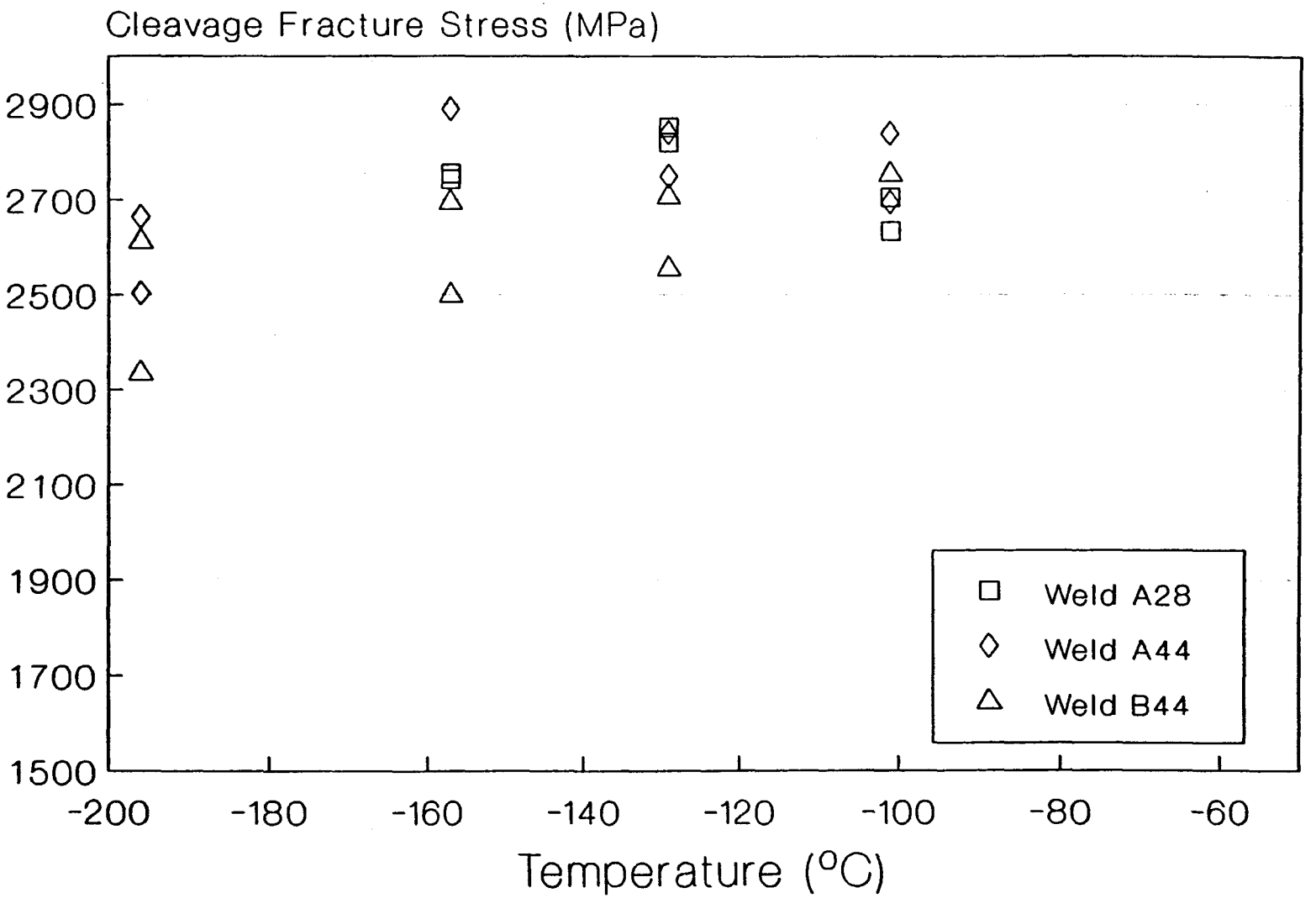

Fig. 21. Cleavage fracture stress, σ_c, versus temperature for welds A28, A44, and B44.

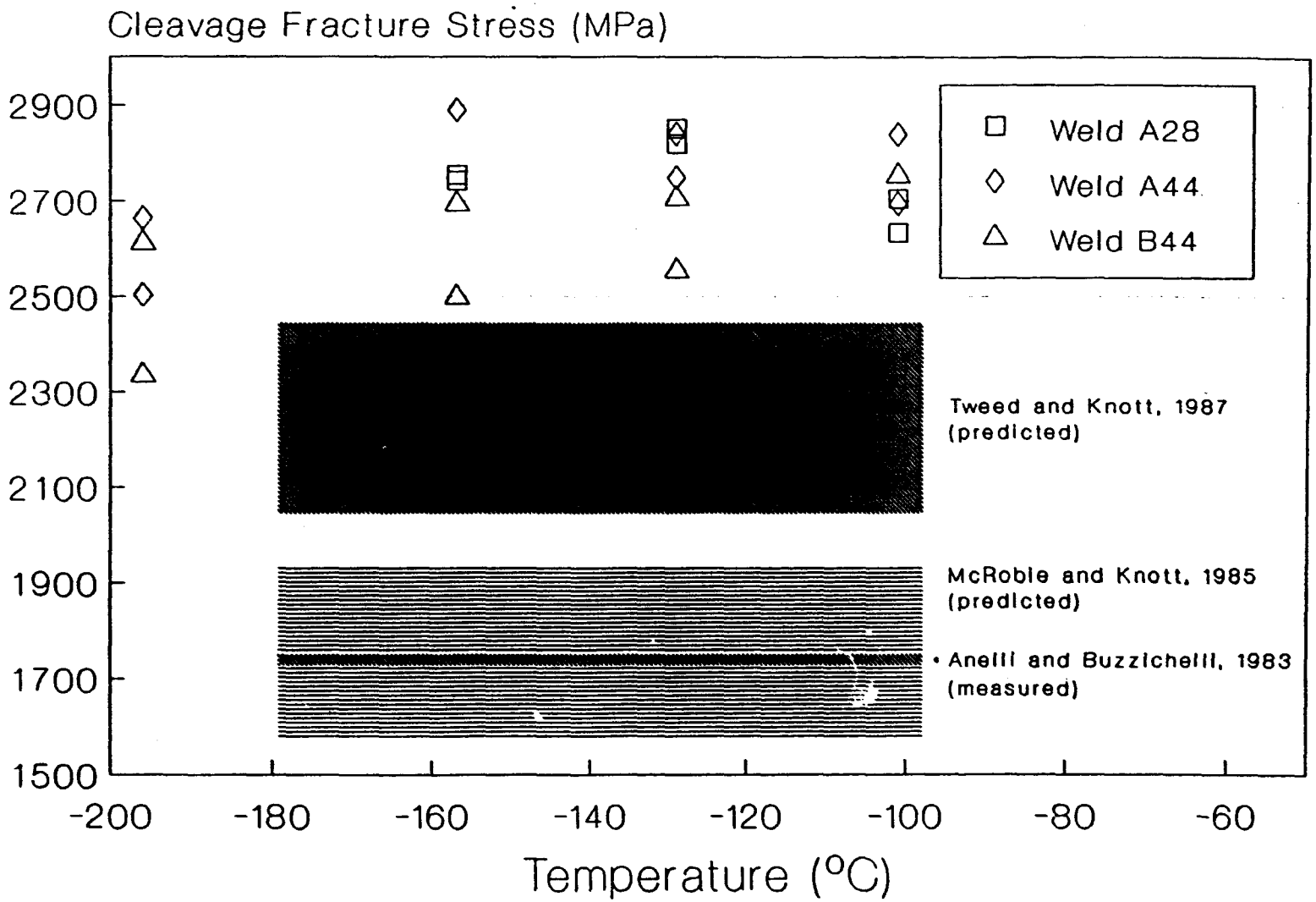

Fig. 22. Comparison of σ_c data from welds A28, A44, and B44 with data generated in the literature.

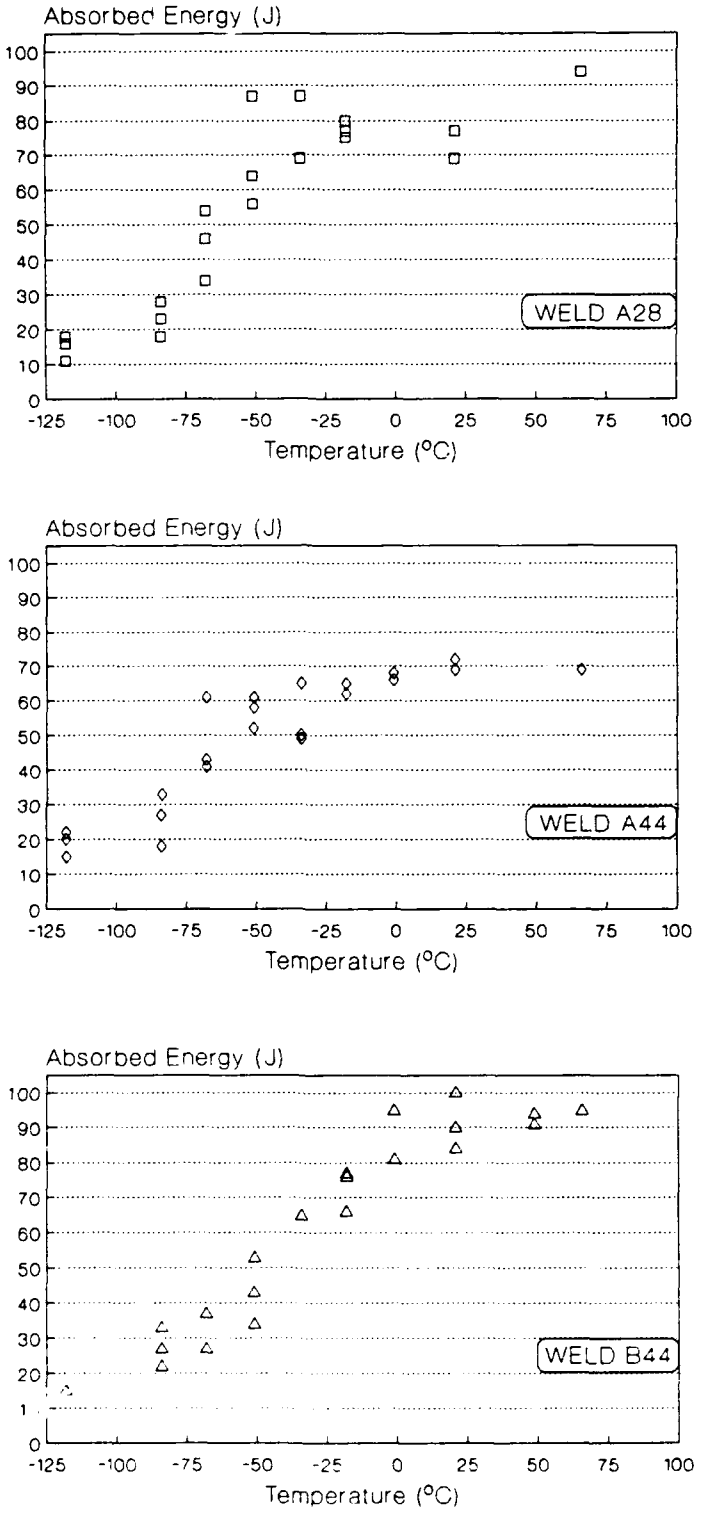

Fig. 23. Charpy V-notch absorbed energy versus temperature for welds A28, A44, and B44.

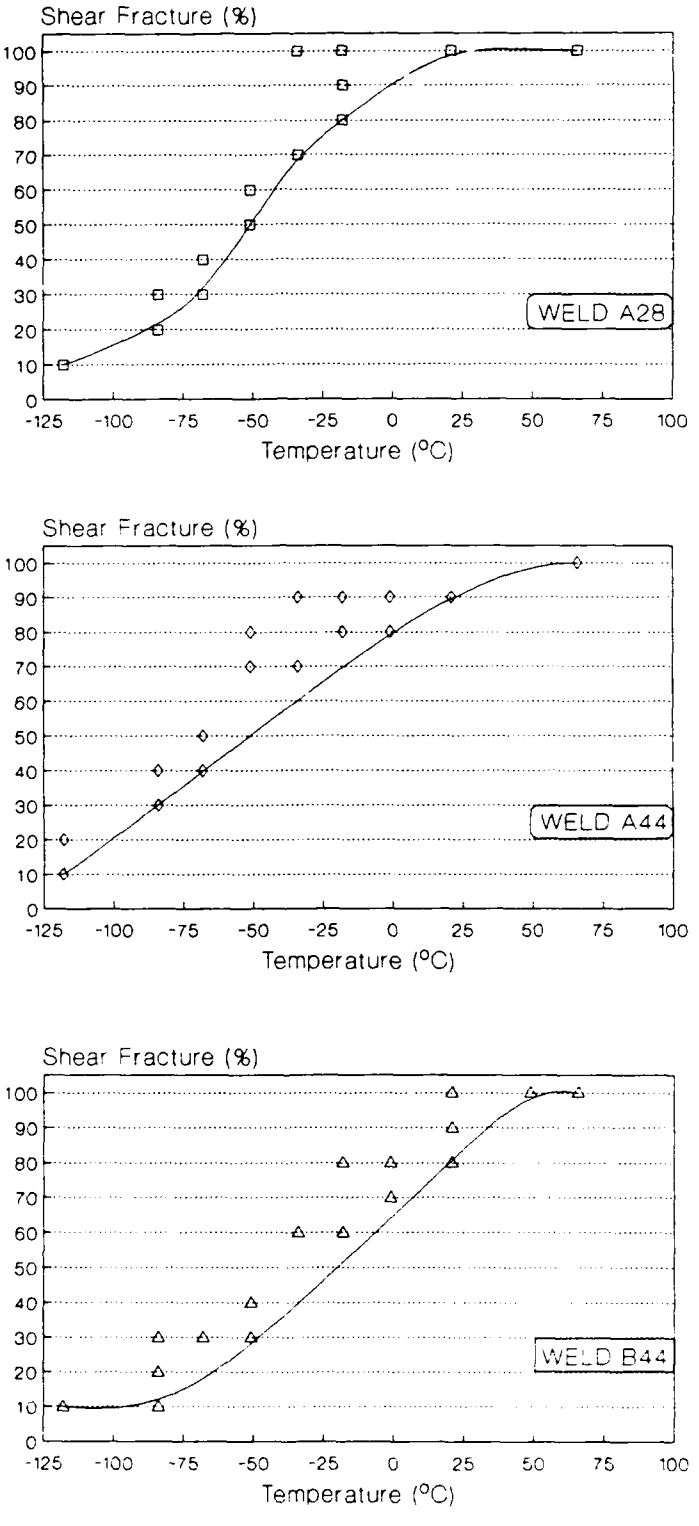

Fig. 24. Percent shear fracture versus temperature for welds A28, A44, and B44.

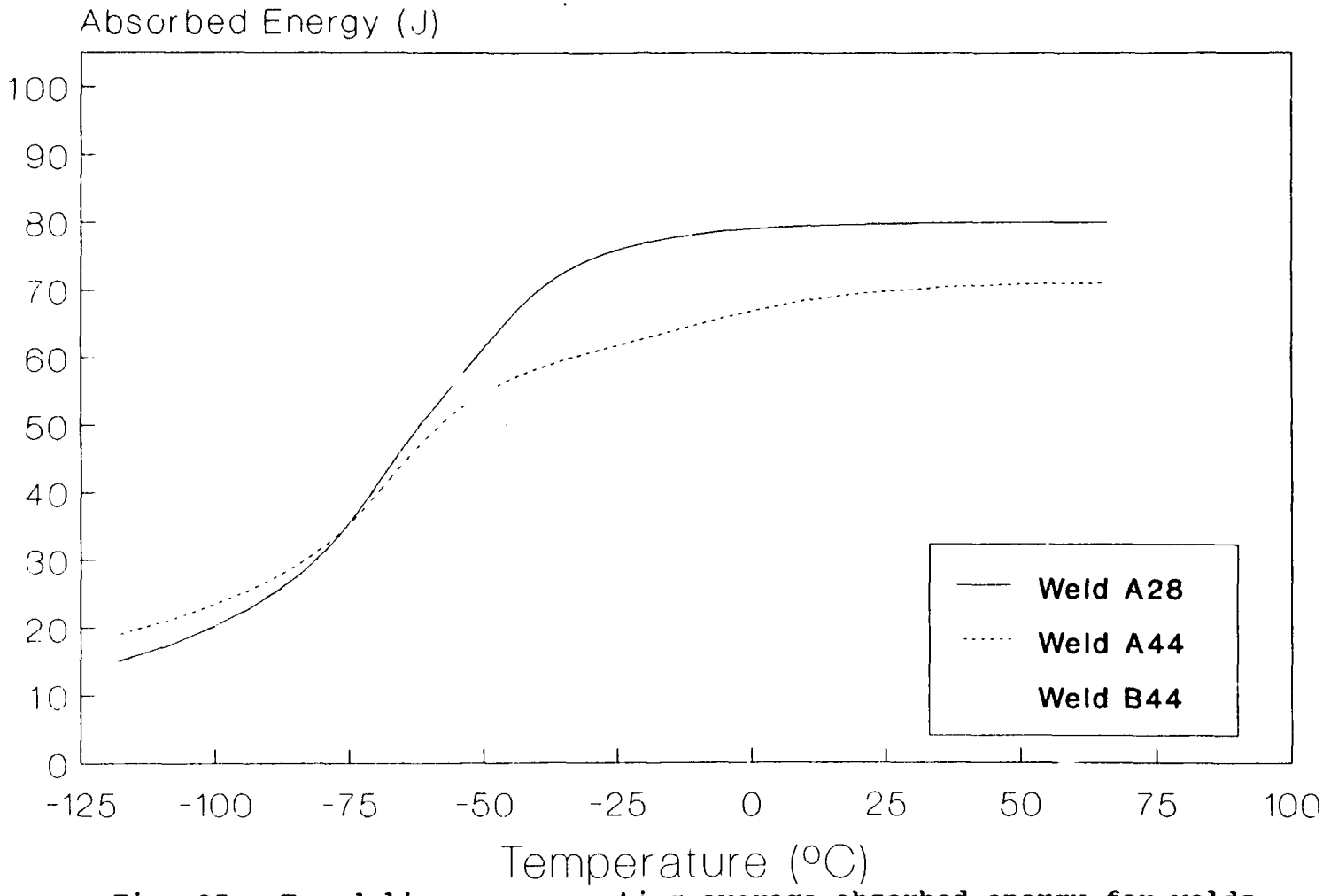

Fig. 25. Trend lines representing average absorbed energy for welds A28, A44, and B44.

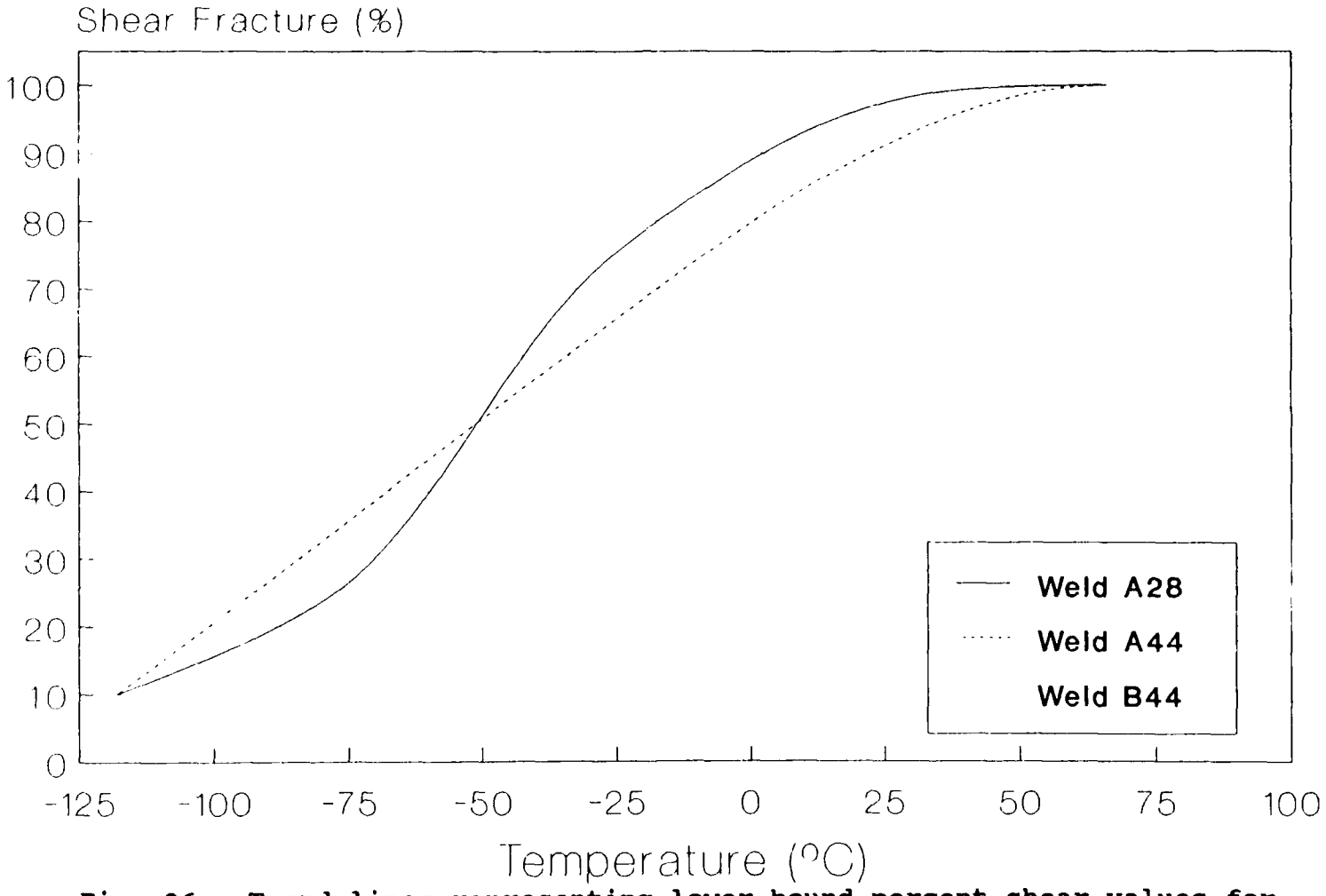

Fig. 26. Trend lines representing lower bound percent shear values for welds A28, A44, and B44.

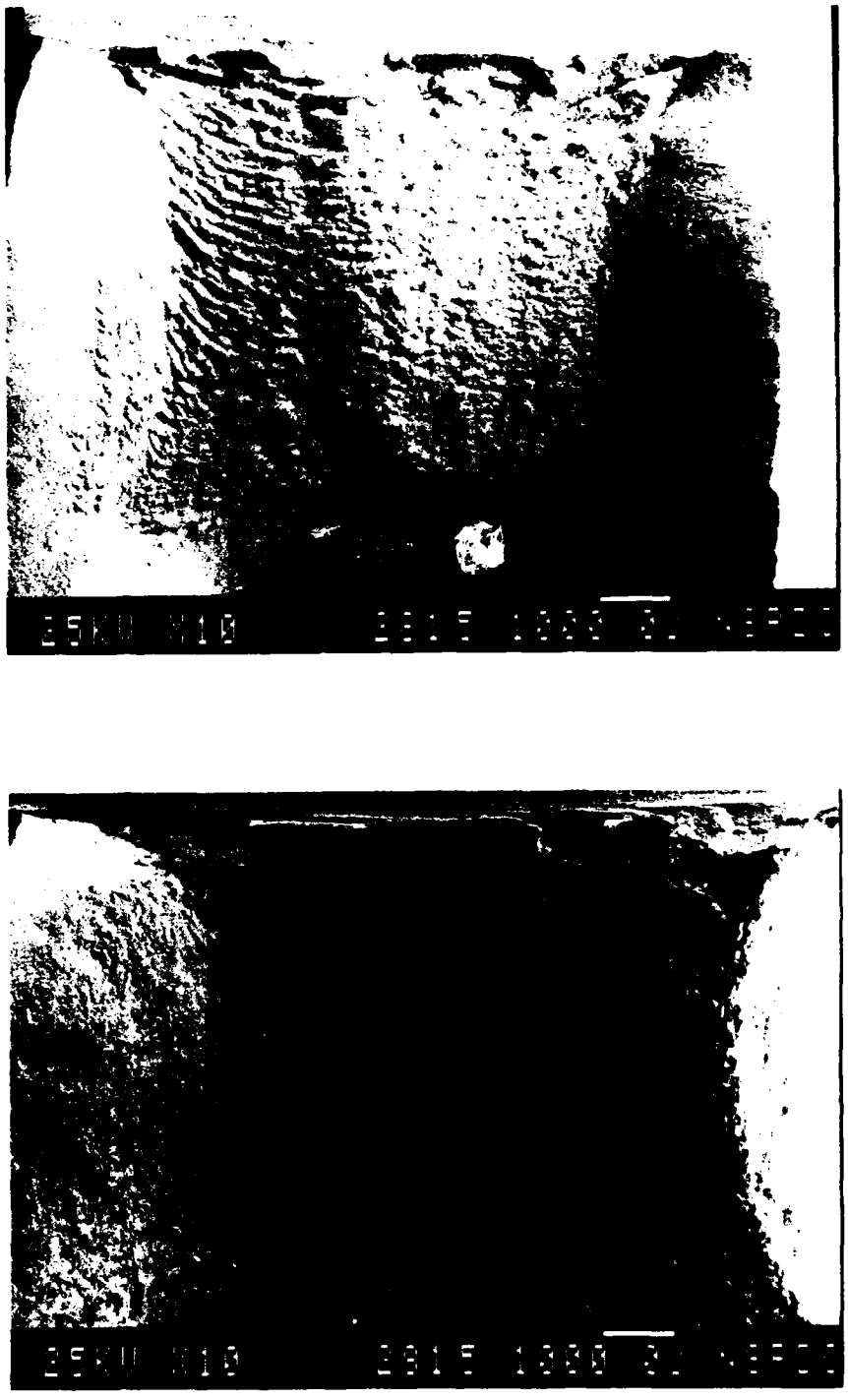

Fig. 27. Low magnification scanning electron fractographs illustrating the striated appearance of the fracture surfaces of CVN specimens tested within the upper shelf region (Top-Specimen A28-41; Bottom-Specimen B44-9).

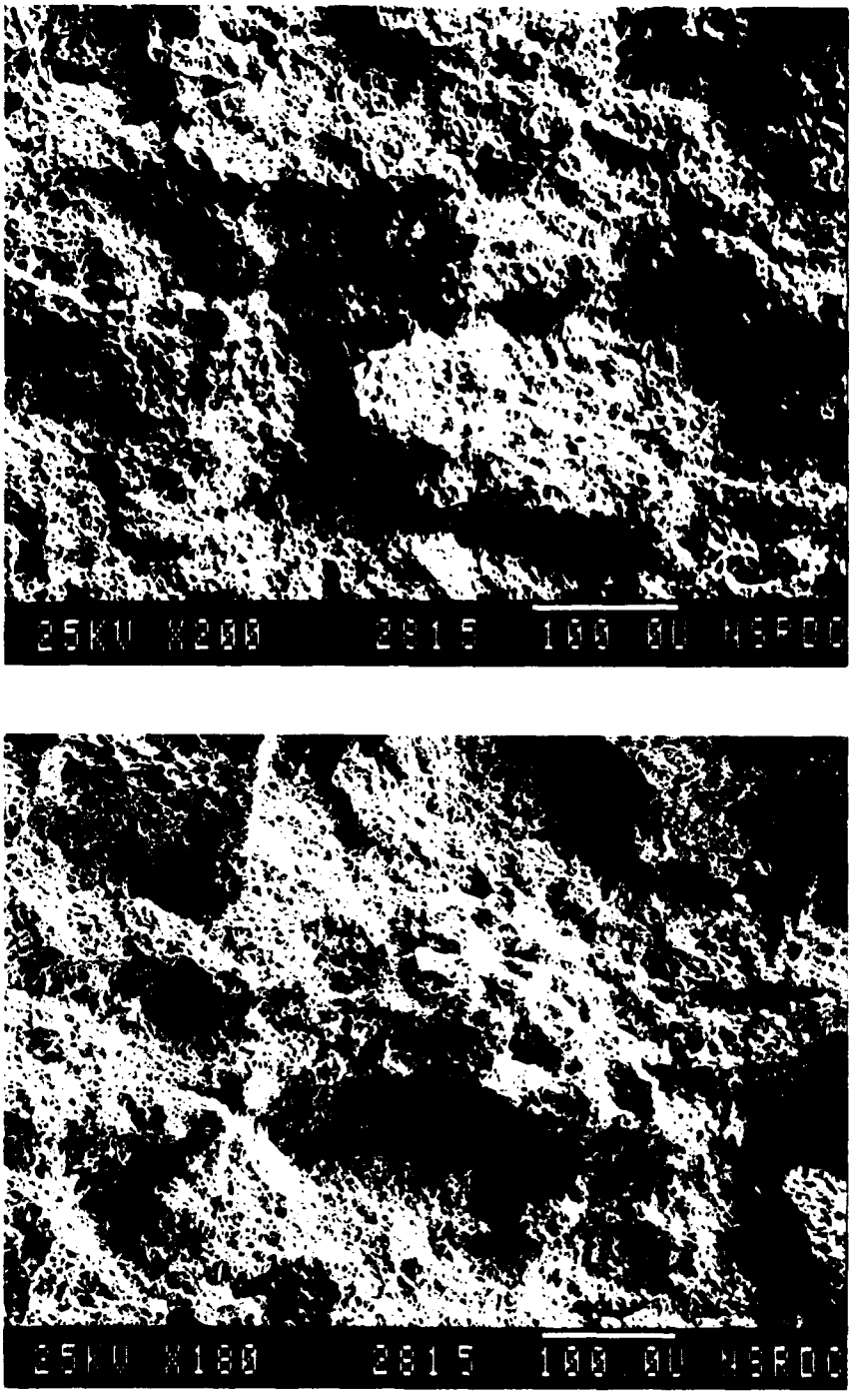

Fig. 28. High magnification scanning electron fractograph of CVN fracture surfaces within the upper shelf region (Top-Specimen A28-41; Bottom-Specimen B44-9).

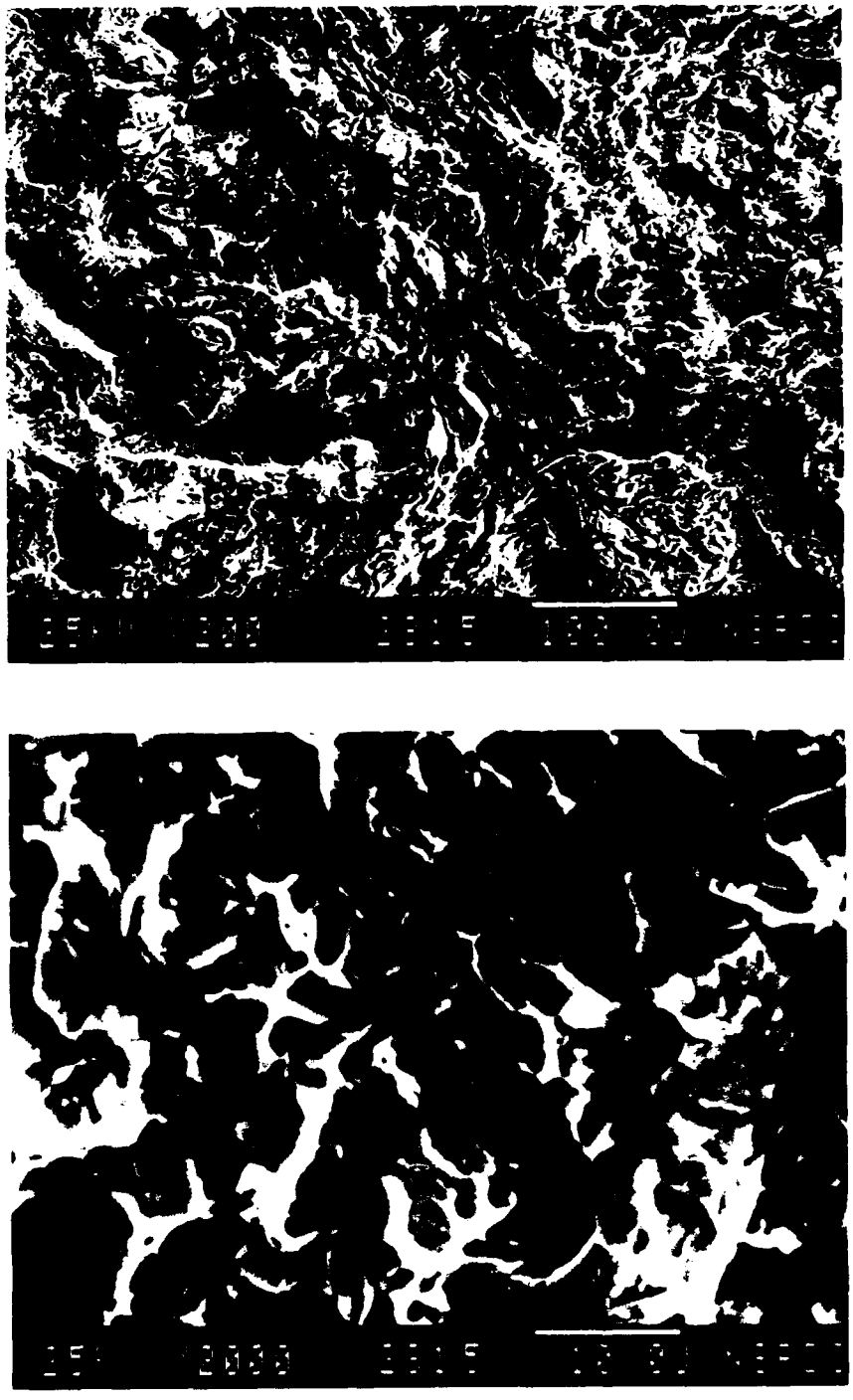

Fig. 29. Scanning electron fractograph illustrating typical appearance of quasicleavage fracture on CVN specimens tested within the lower transition and lower shelf regions (Specimen B44-27).

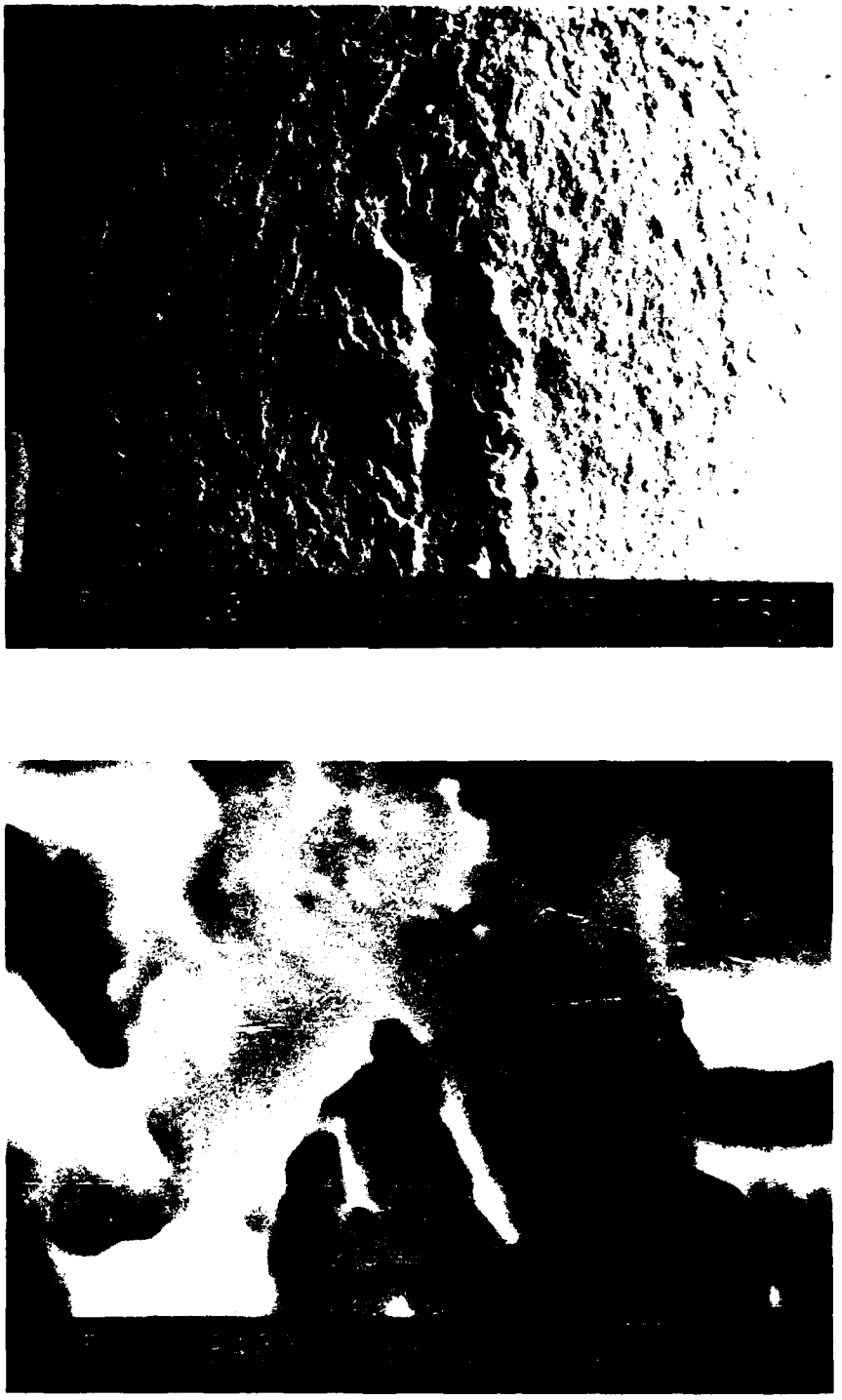

Fig. 30. Example of inclusion-initiated fracture in a notched bend specimen from weld A44 (Specimen A44-5).

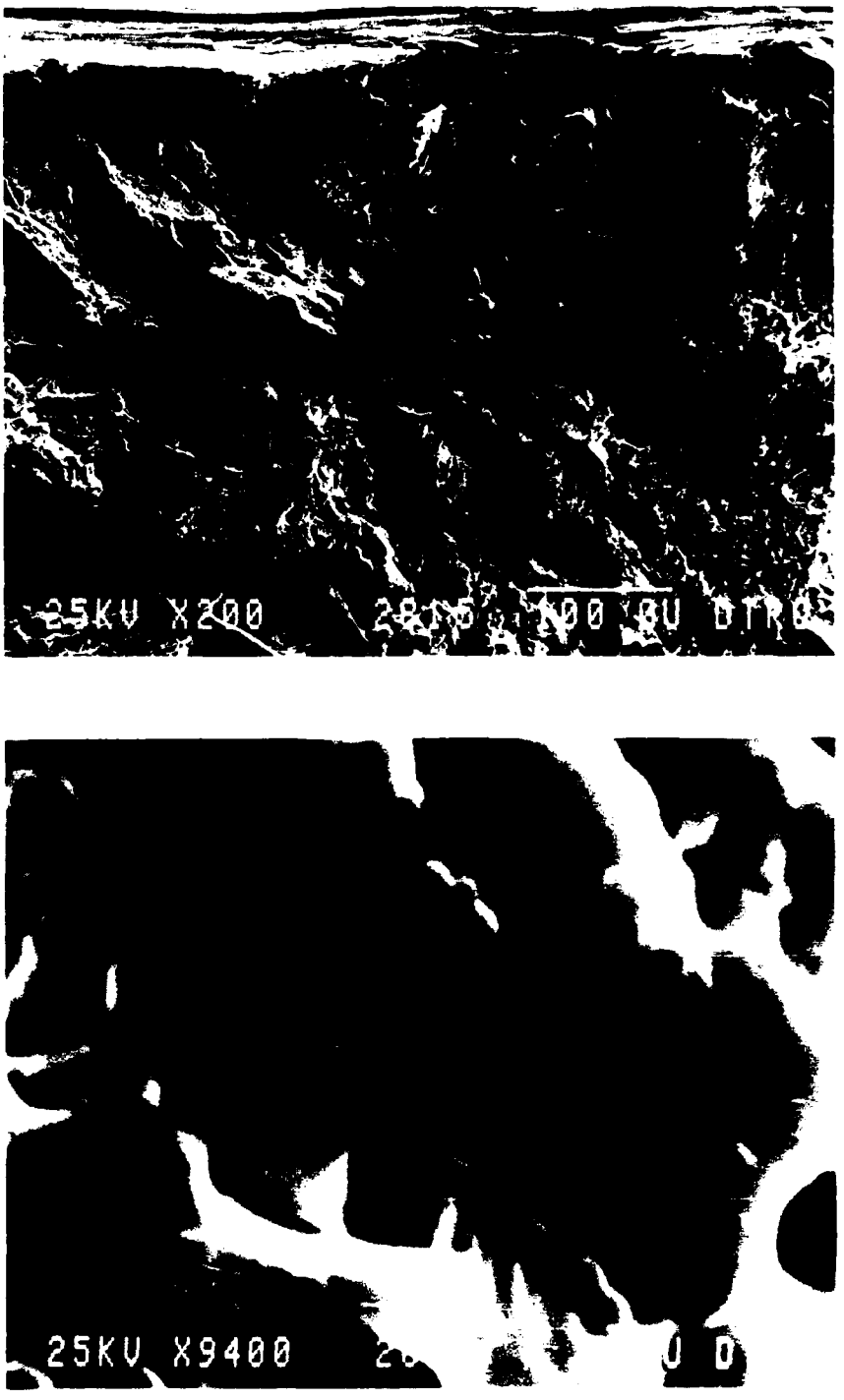

Fig. 31. Example of inclusion-initiated fracture of a notched bend specimen from weld B44 (Specimen B44-27).

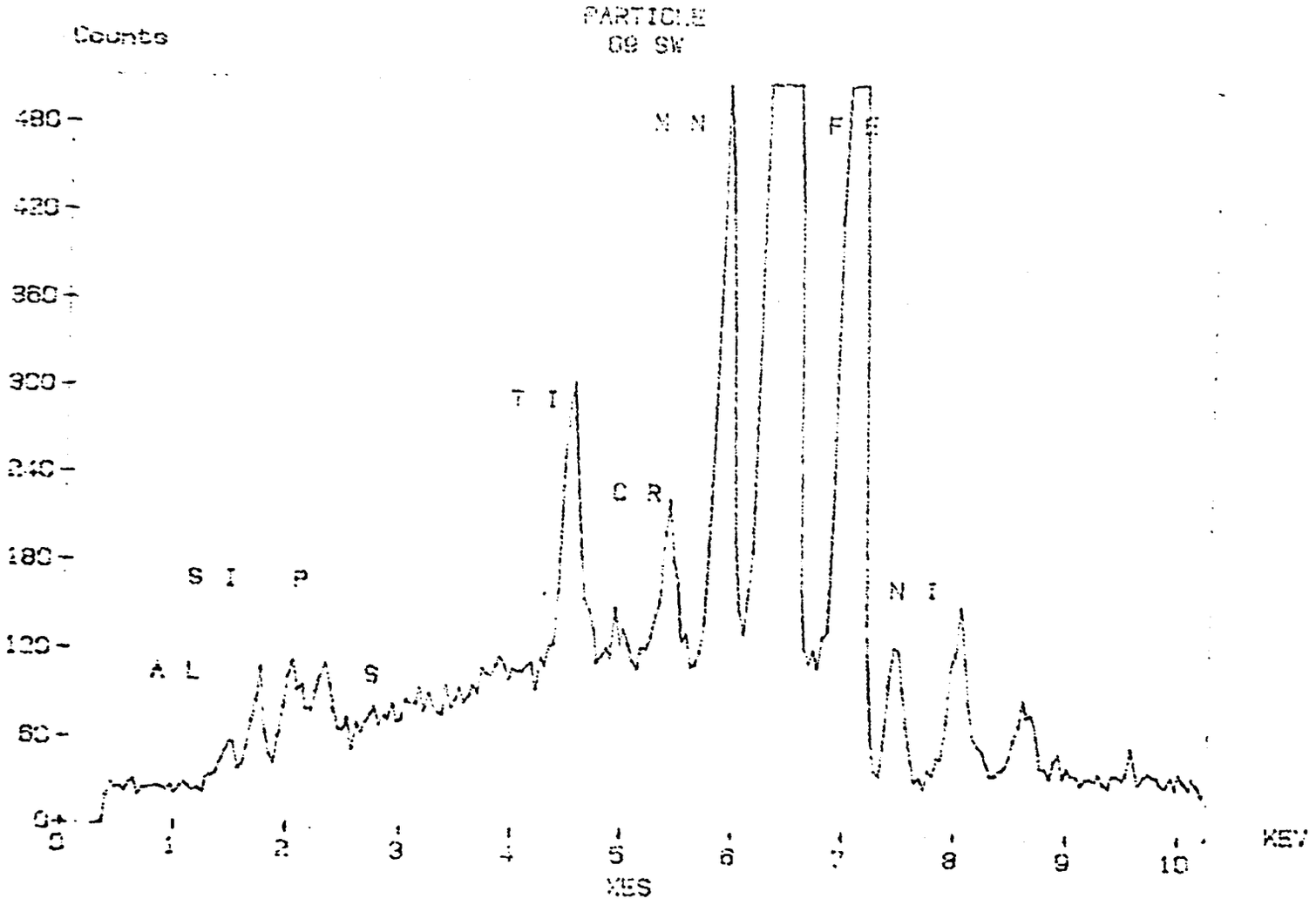

Fig. 32. Energy dispersive x-ray spectrum of fracture-initiating inclusion in notched bend specimen from weld B44 (same inclusion shown in Fig. 31).

APPENDIX A

PROCEDURE FOR CALCULATING LOWER BOUND ESTIMATES USING LOG-NORMAL STATISTICS [Ang and Tang, 1975]

1. Convert all σ_c data to log values.
2. For each data set (welds A28, A44, and B44), calculate the average (avg) and standard deviation (s.d.) of the log values.
3. Select a confidence level (90% for this study).
4. Find the t-statistic for each data set (based on degrees of freedom and confidence level).
5. Perform the following calculation:

   log lower bound σ_c = avg - [(s.d.)(t-statistic)]
6. Calculate the inverse log of each value generated in 5.

APPENDIX B

METHOD FOR CALCULATING INCLUSION CONTENT (VOL. %) FROM WELD METAL COMPOSITION [Bailey, 1978]

1. Assume all sulfur (S) goes to manganese sulfides (MnS):

   MnS (vol. %) = S (wt. %) x 5.3

2. Assume all titanium (Ti) combines with oxygen (O) to form titanium oxides (TiO_2):

   TiO_2 (vol. %) = Ti (wt. %) x 3.67; oxygen consumed = 0.67Ti

3. Assume that oxygen remaining after step 2. combines with aluminum to form aluminum oxides (Al_2O_3):

   Al_2O_3 (vol. %) = Al (wt. %) x 4.09; oxygen consumed = 0.89Al

4. Assume that all remaining oxygen forms manganese silicates ($2MnO \cdot SiO_2$):

   $2MnO \cdot SiO_2$ (vol. %) = remaining O (wt. %) x 6.4

REFERENCES

K.W. Andrews, J. Iron Steel Inst., 203, p. 721, 1965.

E. Anelli and G. Buzzichelli, in "Structure-strength-toughness Relations in the Fusion Zone Depending on Chemical Compositions and Welding Method", Contract no. 7210-KE/405, Centro Sperimentale Metallurgico SpA, 1983.

A.H.S. Ang and W.H. Tang, Probability Concepts in Engineering Planning and Design, Volume 1 - Basic Principals, John Wiley & Sons, 1975.

R.W. Armstrong, Phil. Mag., 9, p. 1063, 1964.

R.W. Armstrong, Acta Metall., 25, p. 667, 1967.

R.W. Armstrong, L. Roberson Link, and G.R. Speich, PROCESSING, MICROSTRUCTURE AND PROPERTIES OF HSLA STEELS, edited by A.J. DeArdo (The Metallurgical Society of AIME), 1988.

N. Bailey, Welding Institute Research Report 70/1978, 1978.

P. Bowen and J.F. Knott, Met. Sci., 18, p.225, 1984.

P. Bowen and J.F. Knott, Metall. Trans. A, 17A, pp. 231, 1986.

P. Brozzo, G. Buzzichelli, A. Masconzoni, and M. Mirabile, Met. Sci., 11, p. 123, 1977.

C. Chen, A.W. Thompson, and I.M. Bernstein, in WELDMENTS: PHYSICAL METALLURGY AND FAILURE PHENOMENA, edited by R.J. Christoffel, E.F. Nippes, and H.D. Solomon (Proceedings of the 5th Bolten Landing Conference), p. 219, 1978.

J.H. Chen and C. Yan, Mat. Sci. and Tech., 4, p. 732, 1988.

C.G. Chipperfield and J.F. Knott, Met. Tech., 2, p. 45, 1975.

L.P. Conner, A.M. Rathbone, and J.H. Gross, Weld. J. Res. Suppl., 46, p. 309s, 1967.

K. Conrad, Mat. Sci. and Eng., 6, p. 265, 1970.

D.A. Curry and J.F. Knott, Met. Sci., 12, p. 511, 1978.

D.A. Curry and J.F. Knott, Met. Sci., 13, p. 341, 1979.

P. Deb, K.D. Challenger, and A.E. Therrien, Metall. Trans. A, 18A, p. 987, 1987.

K.E. Dorschu and A. Lesnewich, Weld. J. Res. Suppl., 43, p. 564s, 1964.

K.E. Dorschu and R.D. Stout, Weld. J. Res. Suppl., 40, p. 97s, 1961.

K.E. Easterling, Introduction to the Physical Metallurgy of Welding, Butterworths, 1983.

A. Enis and R.T. Telford, Weld. J. Res. Suppl., 47, p. 271s, 1968.

A.A. Griffith, Philos. Trans. R. Soc. London, 221A, p. 163, 1920.

J.R. Griffiths and D.R.J. Owen, J. Mech. Phys. Sol., 19, p.419, 1971.

J.P. Gudas, Micromechanisms of Fracture and Crack Arrest in Two High Strength Steels, Ph. D. Thesis, Johns Hopkins University, 1985.

Y. Hagiwara and J.F. Knott, in ADVANCES IN FRACTURE RESEARCH (FRACTURE 81), p. 707, 1981.

E.O. Hall, Proc. Phys. Soc. London, 643, p. 747, 1951.

D.F. Hasson, D. and C.A. Zanis, and D.R. Anderson, Weld. J. Res. Suppl., 63, p. 197s, 1984.

P.W. Holsberg, in Microalloying 1988, (Proceedings of the Internsational Symposium on Application of HSLA Steel), 1988.

F.P.L. Kavishe and T.J. Baker, Mat. Sci. and Tech., 2, p.583, 1986.

M.T. Kirk, presented at The Materials' Properties Council Workshop on Underatanding Scatter of Fracture Toughness Data in the Transition Regime, 1987.

J.F. Knott, J. Iron Steel Inst., 204, p. 104, 1966.

J.F. Knott, J. Iron Steel Inst., 205, p. 966, 1967.

J.F. Knott, Phil. Trans. R. Soc. London, A299, p. 45, 1981.

B.M. Krantz, Weld. J. Res. Suppl., 50, p. 235s, 1971.

S.J. Mangello, D.S. Dabkowski, L.F. Porter, and J.H. Gross, Weld. J. Res. Suppl., 43, p. 514s, 1964.

K. Masabuchi, R.E. Monroe, and D.C. Martin, Weld. Res. Coun. Bull., 111, 1966.

C.J. McMahon, Jr. and M. Cohen, Acta Metall., 13, p. 591, 1965.

D.E. McRobie and J.F. Knott, Mat. Sci. and Tech., 1, p. 357, 1985.

O. Nakayama, H. Nakana, and H. Tashiko, The Welding World, 20, p.509, 1968.

J.P. Naylor, Metall. Trans. A, 10A, p. 861, 1979.

G. Oates, J. Iron Steel Inst., 207, p. 353, 1969.

P.T. Oldland, The Effects of Heat Input and Molybdenum Content on the Microstructures and Mechanical Properties of High Strength Steel Weld Metal, M.S. Thesis, Colorado School of Mines, 1988.

E. Orowan, Trans. Inst. Eng. Shipbuild. Scot., 89, p. 165, 1945.

E. Orowan, in Fatigue and Fracture of Metals, (Symposium at Massachusetts Institute of Technology), 1952.

N.J. Petch, J. Iron Steel Inst., 64B, p.747, 1953.

D.J. Peters, Submerged Arc Welding Consumables for HSLA-100 Steel, M.S. Thesis, Massachusetts Institute of Technology, 1989.

C.W. Ramsey, D.K. Matlock, and D.L. Olson, presented at 2nd International Conference on Trends in Welding Research, 1989.

R. Sandstrom and Y. Bergstrom, Met. Sci., 18, p. 177, 1984.

G.G. Saunders, Weld. Res. Int., 7, p. 91, 1977.

E. Smith, in PROCEEDINGS OF CONFERENCE ON PHSYSICAL BASIS OF YIELD AND FRACTURE (Institute of Physics and Physical Soc., Oxford) p. 36, 1966.

S.S. Strunck and R.D. Stout, Weld. J. Res. Suppl., 52, p. 508s, 1972.

J.H. Tweed and J.F. Knott, Met. Sci., 17, p. 45, 1983.

J.H. Tweed and J.F. Knott, Metal Construction, 19, p. 153R, 1987.

P.G. Winchell and M. Cohen, Trans. Met. Soc. AIME, 224, p. 638, 1962.

X.J. Zhang, R.W. Armstrong, and G.R. Irwin, J. Mat. Sci. Letters, 5, p. 961, 1986.

INITIAL DISTRIBUTION

CENTER DISTRIBUTION

Copies		Copies	Code
		1	0115
24	NAVSEA	1	172
		1	173
1	SEA 05M	1	28
1	SEA 05MB	1	2801 (JRC)
1	SEA 05M2	1	2801 (DRV)
1	SEA 05R	1	2802 (ASGM)
1	SEA 05R25	1	2803 (JLC)
1	SEA 05R26	1	2809 (AAM)
1	SEA 08	1	28
1	SEA 55Y	5	281
1	SEA 55Y1	1	2814
1	SEA 55Y2	1	2814 (MGV)
1	SEA 55Y21	1	2814 (DM)
1	SEA 55Y22	1	2814 (SJM)
1	SEA 55Y23	1	2814 (MTK)
1	SEA 55Y3	2	2815
1	SEA 55Y31	1	2815 (GLF)
1	SEA 55Y32	1	2815 (RJW)
1	SEA 92R	10	2815 (JJD)
1	PMS 350	1	2815 (RTB)
1	PMS 392	1	2815 (RHJ)
1	PMS 393	1	283
1	PMS 394	1	284
1	PMS 396	1	5221
2	SEA 99612	1	5222
		2	5231
12	DTIC		

1 Chief of Naval Research
Office of Naval Technology
Attn: Mr. M. Kinna (OCNR 225)
800 N. Quincy Street
Arlington, VA 22217

1 Supervisor of Shipbuilding Conversion and Repair, USN General Dynamics Corporation
Electric Boat Division
Dept. 341
Groton, CT 06340

1 Supervisor of Shipbuilding Coversion and Repair, USN Newport News Shipbuilding
Dept. 037
Newport News, VA 23607